

# ON THE ACCRETION ORIGIN OF A VAST EXTENDED STELLAR DISK AROUND THE ANDROMEDA GALAXY

R. IBATA<sup>1</sup>, S. CHAPMAN<sup>2</sup>, A. M. N. FERGUSON<sup>3</sup>, G. LEWIS<sup>4</sup>, M. IRWIN<sup>5</sup>, N. TANVIR<sup>6</sup>

*Draft version February 2, 2008*

## ABSTRACT

We present the discovery of an inhomogenous, low-surface brightness, extended disk-like structure around the Andromeda galaxy (M31) based on a large kinematic survey of more than 2800 stars with the Keck/DEIMOS multi-object spectrograph. The stellar structure spans radii from 15 kpc out to  $\sim 40$  kpc, with detections out to  $R \sim 70$  kpc. The constituent stars lag the expected velocity of circular orbits in the plane of the M31 disk by  $\sim 40$  km s<sup>-1</sup> and have a velocity dispersion of  $\sim 30$  km s<sup>-1</sup>. The color range on the upper RGB shows a large spread indicative of a population with a significant range of metallicity. The mean metallicity of the population, measured from Ca II equivalent widths, is  $[Fe/H] = -0.9 \pm 0.2$ . The morphology of the structure is irregular at large radii, and shows a wealth of substructures which must be transitory in nature, and are almost certainly tidal debris. The presence of these substructures indicates that the global entity was formed by accretion. This extended disk follows smoothly on from the central parts of M31 disk out to  $\sim 40$  kpc with an exponential density law of scale-length of  $5.1 \pm 0.1$  kpc, which is similar to that of the bright inner disk. However, the population possesses similar kinematic and abundance properties over the entire region where it is detected in the survey. We estimate that the structure accounts for approximately 10% of the total luminosity of the M31 disk, and given the huge scale, contains  $\sim 30\%$  of the total disk angular momentum. This finding indicates that at least some galactic stellar disks are vastly larger than previously thought and are formed, at least in their outer regions, primarily by accretion.

*Subject headings:* galaxies: individual (M31) — galaxies: structure — galaxies: evolution — Local Group

## 1. INTRODUCTION

Within the framework of hierarchical structure formation, large spiral galaxies like the Milky Way or Andromeda (M31) arose from the merger of many small galaxies and protogalaxies which began coalescing at high redshift. During this process, considerable dynamical and chemical evolution took place, as the primordial galaxy fragments were assimilated, stellar populations evolved and fed enriched gas back into the interstellar medium, and fresh gas was accreted onto the galaxy. The disk, the defining component of spiral galaxies, formed through dissipative processes, growing from the inside out mainly by the accretion of gas with high angular momentum with probably only a small component of accreted stars (Abadi et al. 2003).

The structure of disks is generally exponential in both their radial and vertical directions. A striking feature of this component of galaxies is the tendency for it to be truncated radially at 3–4 scale-lengths (van der Kruit & Searle 1981; Pohlen, Dettmar & Lütticke 2000). This distance would correspond to  $\sim 12$  kpc in the Milky Way and  $\sim 20$  kpc in M31. Although we still lack a solid understanding of how and why these truncations occur,

evidence suggests an abrupt change in the star formation efficiency across this boundary, perhaps related to a shift in the dominant star formation mode (Kennicutt 1989; Ferguson et al. 1998; Schaye 2004). The fact that disk stars are detected beyond the predicted truncation radii in the Milky Way and M31, as well as in several lower mass galaxies (e.g. NGC 300, Bland-Hawthorn et al. 2005; M33, Ferguson et al 2005, in prep), is intriguing. Did these stars form *in situ*? If so, did they form a long time ago during the very early stages of disk evolution, or have they formed much more recently from newly-acquired gas? On the other hand, could they have been tidally stripped from infalling satellites on close to coplanar orbits?

In order to address these questions and examine galaxy formation models in detail, our group has undertaken a deep panoramic study of the Andromeda galaxy, which when set in contrast with the Milky Way, was to serve as a test case against which formation simulations could be compared. Studies of the Milky Way are naturally blessed with more photons than those of more distant systems, and by resolving individual stars and measuring their kinematic and chemical properties one can study the formation of our Galaxy in a detail and with a mass and spatial resolution that can only be dreamed of elsewhere. However, thanks to advances in instrumentation, it is now also possible to measure the kinematics and chemistry of individual stars in galaxies of the Local Group. One of the major benefits that this affords us is a global view of a galaxy, freeing us from much of the projection uncertainties that our position within the Milky Way plagues us with, and yet retaining the fine detail that spectroscopic studies of resolved stellar populations

<sup>1</sup> Observatoire de Strasbourg, 11, rue de l'Université, F-67000, Strasbourg, France

<sup>2</sup> California Institute of Technology, Pasadena, CA, 91125

<sup>3</sup> Institute for Astronomy, University of Edinburgh, Royal Observatory, Blackford Hill, Edinburgh, UK EH9 3HJ

<sup>4</sup> Institute of Astronomy, School of Physics, A29, University of Sydney, NSW 2006, Australia

<sup>5</sup> Institute of Astronomy, Madingley Road, Cambridge, CB3 0HA, U.K.

<sup>6</sup> Physical Sciences, Univ. of Hertfordshire, Hatfield, AL10 9AB, UK

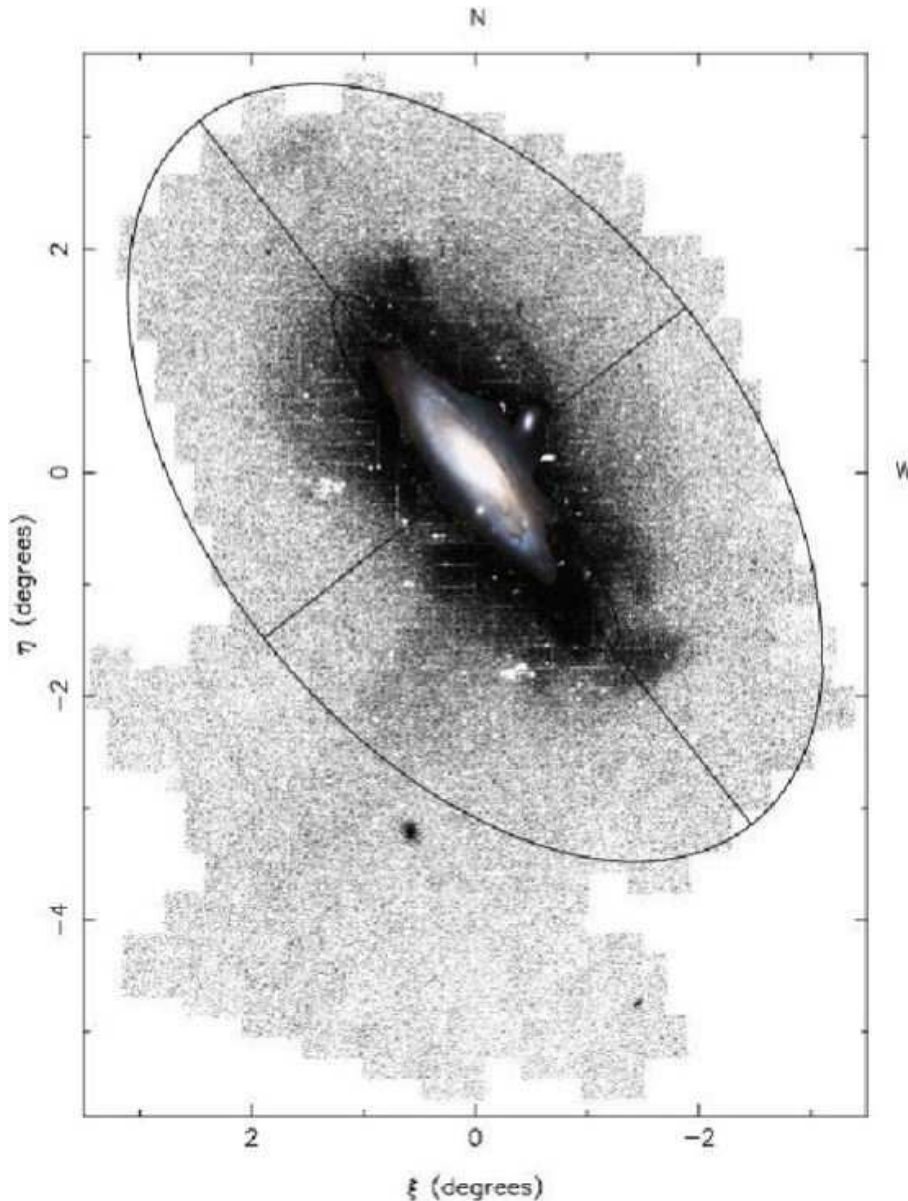


FIG. 1.— The current coverage of our large panoramic survey of M31 with the INT camera, in standard coordinates  $(\xi, \eta)$ . The outer ellipse shows a segment of a 55 kpc radius ellipse flattened to  $c/a = 0.6$ , and the major and minor axis are indicated with straight lines out to this ellipse. A DSS image of the central galaxy has been inserted to scale. The map shows the distribution of RGB stars throughout the halo. The most striking structure in the map is a vast flattened inner structure, of major axis extent  $\sim 4$  degrees, a messy inhomogeneous entity which envelops the familiar bulge and disk of M31.

provide.

Located at a distance of  $785 \pm 25$  kpc ( $(m - M)_0 = 24.47 \pm 0.07$ ; McConnachie et al. 2005), Andromeda is the closest giant spiral galaxy to our own, and the only other giant galaxy in the Local Group. As such it is often considered to be the “sister” galaxy to the Milky Way. Recent studies suggest that the two galaxies do indeed have very similar total masses (including the dark matter, Evans et al. 2000; Ibata et al. 2004), yet there are significant differences between them. M31 is slightly more luminous than the Milky Way, it has a higher rotation curve, and a bulge with higher velocity dispersion. M31 possesses and a globular cluster system with  $\sim 500$  members, approximately three times more nu-

merous than that of the Milky Way, and contains several members of a type of luminous extended cluster not present around the Galaxy (Huxor et al. 2005). The disk of Andromeda is also much more extensive, with a scale-length of  $5.9 \pm 0.3$  kpc (R-band value corrected for a distance of 780 kpc, Walterbos & Kennicutt 1988) compared to  $2.3 \pm 0.1$  for the Milky Way (Ruphy et al. 1996); but which is currently forming stars at a lower rate than the Galaxy (Avila-Reese, Firmani & Hernández 2002; Walterbos & Braun 1994). Though possibly the consequence of low-number statistics, it is tempting to attribute significance to the fact that Andromeda has four dwarf elliptical galaxies (M32, NGC 205, NGC 147, NGC 185) among its entourage of satellites and no star-

forming dwarf irregulars, whereas the Milky Way has none of the former but two of the latter. However, it is perhaps in their halo populations that the differences between the two galaxies are most curious and most interesting. It has been known for many years that M31 does not possess the “text-book” stellar halo model developed from observations of the Milky Way. Minor axis halo fields have shown startlingly high metallicities ( $[\text{Fe}/\text{H}] \sim -0.5$ ) and an  $R^{1/4}$ -law density profile (Durrell, Harris & Pritchet 2004), unlike the  $R^{-3.5}$  behavior of the metal-poor Galactic halo (Chiba & Beers 2000). Nevertheless, recent studies of M31 confirm that an old, metal-poor halo lurks beneath (Holland 1996; Durrell, Harris & Pritchet 2001; Reitzel & Guhathakurta 2002; Brown et al. 2003). Both the de Vaucouleurs profile and the high metallicity are suggestive of an active merger history at the time of halo (or bulge) formation.

The photometric dataset that forms the foundation of this study was obtained with the Wide Field Camera at the 2.5m Isaac Newton Telescope; the survey and preliminary results were presented in Ibata et al. (2001b) and Ferguson et al. (2002), though the full completed survey will be discussed in detail in a forthcoming article (Irwin et al., in prep). The density of Red Giant Branch (RGB) stars throughout the survey region, which now covers  $\sim 40$  sq. degrees, is reproduced in Figure 1, onto which we have superimposed the familiar Digital Sky Survey image. The solid angle covered by the survey corresponds to a projected area of  $\sim 7400 \text{ kpc}^2$  at the distance of M31. As shown in the earlier publications in this series, the INT survey revealed a wealth of substructure throughout the “halo” of M31. However, the most prominent of the details that we uncovered was the presence of a gigantic extended flattened structure around M31, spanning up to  $\sim 40$  kpc from the galaxy centre, almost twice the maximum extent of the bright inner disk. Due to the expectations from galaxy formation simulations with cold dark matter, our initial interpretation of this structure favored the possibility that it was a flattened inner halo (Katz & Gunn 1991; Summers 1993; Steinmetz & Müller 1995) with significant spatial sub-structure (Klypin et al. 1999; Moore et al. 1999). However, the proximity of M31 has allowed us to follow up these detections with deep Keck/DEIMOS spectroscopic observations (initial results of the spectroscopic survey were presented in Ibata et al. 2004). It is the radial velocities and metallicities derived from these deep spectroscopic data that we present and analyze in this contribution.

The layout of this paper is as follows. In §2 we first discuss the global geometry of M31, the inclination angle of the disk and fit an exponential function to the major axis photometry. The spectroscopic observations are presented in §3, and the resulting kinematics in §4. In §5 we examine several fields in more detail, presenting also their mean metallicity and fitting global trends. These data are interpreted in §6, where we present several possibilities for the formation of the structure, and we finish in §7 with the conclusions of the study.

## 2. SIMPLE GLOBAL STRUCTURAL MODEL OF M31

Before describing the observations and analysis of the kinematic dataset, it is useful to discuss the large-scale structure of M31. Andromeda is observed highly inclined

to the line of sight with  $i = 77^\circ$  (Walterbos & Kennicutt 1988), and it is seen on the sky with a position angle of  $38^\circ$  East of North (Walterbos & Kennicutt 1987). Within an angular distance of  $90'$  (20.4 kpc), Walterbos & Kennicutt (1988) find a good fit with the sum of a bulge model together with a disk model of R-band scale-length  $5.9 \pm 0.3$  kpc (corrected for a distance of 780 kpc).

To compare these findings to our INT survey, we measure the source density in a color-magnitude box designed to select the brightest RGB stars 1.5 magnitudes below the RGB tip. Sources with I-band magnitudes between  $20.0 < i_0 < 21.5$  and colors  $1.0 < (V - i)_0 < 4.0$  are selected. (The Schlegel et al. 1998 dust maps are used throughout this work to correct the INT photometry for extinction). We correct the star-counts for crowding using the approach of Irwin & Trimble (1984), and subtract a small background count as determined from fields at the edge of the survey.

The de-projected positions of the RGB stars are binned in a polar coordinate grid with  $5^\circ$  azimuthal bins and 0.5 kpc radial bins. The azimuthal counts at a given radius are then medianed together in groups of 5 (i.e. covering  $25^\circ$ ), and we step around the circle in intervals of  $15^\circ$ . The upper panel of Figure 2 shows the 4 profiles within a de-projected angle of  $\pm 35^\circ$  of the major axis (i.e.  $\pm 7.9^\circ$  projected), assuming an inclination of  $i = 77^\circ$ , with the additional thick-lined profile showing the median of all 14 bins of  $5^\circ$  width. Positive radius means that the medianed area is on the North-eastern major axis, and negative radius is on the South-western major axis. The abscissa  $R$  is a de-projected radius, that assumes the stated inclination. The artificial drop in the source counts inside of  $R \sim 18$  kpc is due to crowding.

Evidently the major axis profile is close to exponential; it is fit in the lower panel with a model (dashed line) of scale-length  $5.1 \pm 0.1$  kpc. This scale-length is similar to that of the inner disk, so it appears that the large-scale properties of the outer disk structure follow on smoothly from those of the inner disk.

The upper panel of Figure 3 shows the profiles for all azimuthal bins. The large discrepancies between the different profiles are very obvious, with the less steep profiles corresponding to azimuthal bins towards the minor axis. The higher number densities on the minor axis are largely due to the huge bulge component in M31. Indeed, in the bulge-disk decomposition of Walterbos & Kennicutt (1988), the bulge dominates over the disk at all radii on the minor axis. However, part of this variation may also come from a change in the inclination of the galaxy at large radius. To explore this possibility, we fitted the value of  $i$  by assuming that the most likely inclination is that that has the lowest root mean square dispersion about the median profile in the distance interval  $20 < R < 40$  kpc. The corresponding profiles are shown on the lower panel of Figure 3, together with the medianed profile (thick black line). The fitted inclination angle is  $i = 64.7^\circ$ .

With this smaller inclination, the surface density profiles are now much more similar, yet there are still variations between the profiles of up to a factor of  $\sim 2-3$  at a given radius, due in part to the presence of obvious “lumps”. Fitting the median profile between  $20 < R' < 40$  kpc with an exponential-law yields a scale-length of  $7.8 \pm 0.07$  kpc. This larger scale-length

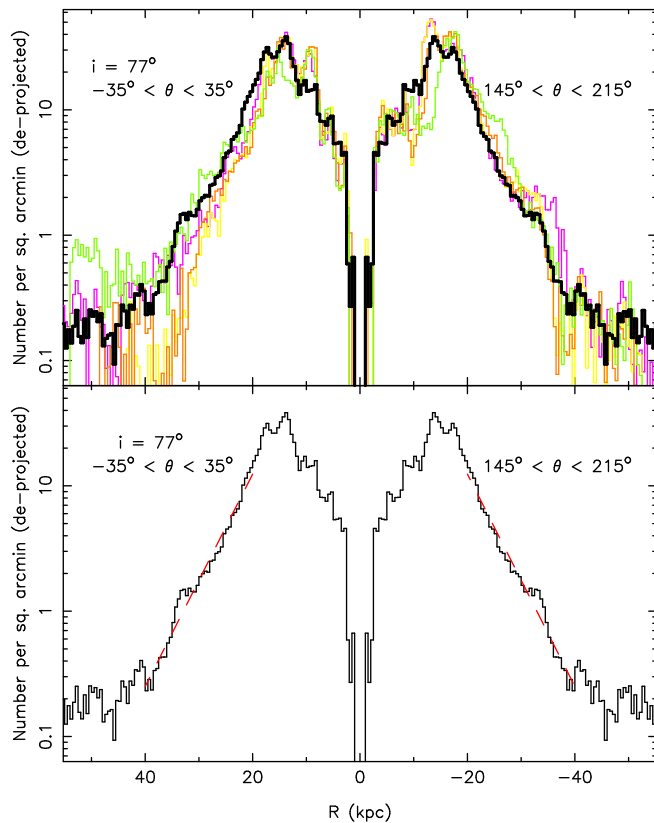


FIG. 2.— The top panel shows the density profiles close to the major axis. Positive abscissa values correspond to de-projected radii towards the North-eastern side of M31. The thin lines are the density profiles medianed over 5  $5^\circ$ -de-projected azimuthal bins, assuming a galaxy inclination of  $i = 77^\circ$ . The 4 profiles to the North-east cover the de-projected angles  $-35^\circ < \theta < 35^\circ$ ,  $-20^\circ < \theta < 5^\circ$ ,  $-5^\circ < \theta < 20^\circ$ ,  $10^\circ < \theta < 35^\circ$ , with the 4 profiles to the South-west being identical cuts rotated by  $180^\circ$ . The thick black line corresponds to the median of all 14 azimuthal bins between  $-35^\circ < \theta < 35^\circ$ . The lower panel shows an exponential fit to the medianed profile between  $20 < R < 40$  kpc, with a scale-length  $5.1 \pm 0.1$  kpc.

value compared to the previous major axis exponential fit demonstrates a failure in our simple tilted disk model. A more complex model with a bulge component is required to fit the central regions of the galaxy more reliably, yet this cannot be constructed from our INT data which are highly incomplete inside of  $R \sim 15$  kpc.

In the following discussion, we will present results based on inclination values of  $i = 77^\circ$  and  $i = 64.7^\circ$ ; this will help clarify the uncertainty due to a possible tilt of the outer disk with respect to the inner disk. De-projected quantities, such as the de-projected radius  $R$  or the velocity lag  $v_{lag}$  (defined below) will implicitly assume an inclination of  $i = 77^\circ$ ; primed versions of these variables (e.g.  $R'$ ,  $v'_{lag}$ ) will instead correspond to the lower inclination case of  $i = 64.7^\circ$ .

### 3. OBSERVATIONS

During eight Keck nights ( $\sim 75\%$  useful time) in Sept. 2002, 2003, and 2004, we undertook a DEIMOS program to spectroscopically follow-up the detected substructures in M31 to measure their kinematics, and to begin a complete kinematic portrait of M31 targeting systematically

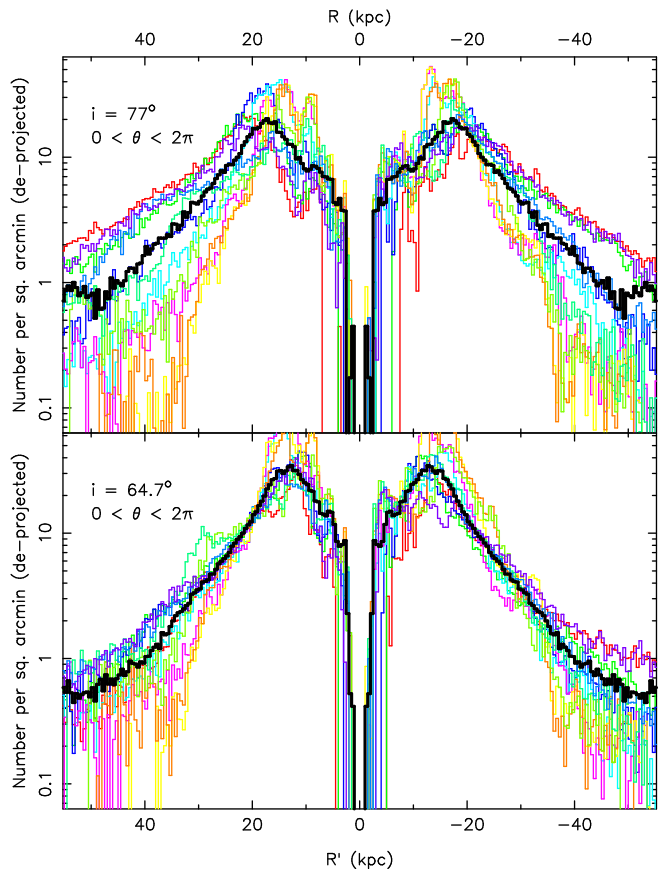


FIG. 3.— The top panel shows medianed density profiles at different position angles around M31, offset at  $15^\circ$  from each other, assuming a galaxy inclination of  $i = 77^\circ$ . As in Figure 2, each profile is constructed from a median of 5 consecutive azimuthal bins of width  $5^\circ$ . The thick black line corresponds to the median of all azimuthal bins. The lower panel shows similar profiles, but for an inclination angle of  $i = 64.7^\circ$ , fitted to minimize the dispersion around the median profile of all azimuthal bins over the interval  $20 < R' < 40$  kpc.

disk and halo fields. The observing runs have employed the standard high-res *DEEP2* slitmask approach (e.g., Davis et al. 2003) covering the wavelength range  $6400\text{--}9000 \text{ \AA}$ , with a spectral resolution of  $\sim 0.6 \text{ \AA}$ . The observations have also pioneered two new approaches with DEIMOS: a band-limiting  $\sim 300 \text{ \AA}$  Ca II triplet filter to multiplex  $\sim 4''$  slitlets in the spectral direction yielding as many as 800 slits per mask, and a ‘fibre-hole’  $0''.7$  slitlet approach packing  $\sim 600$  holes per mask. This ‘fibre-hole’ approach adopted in Sept. 2004 proved to be very successful, giving Poisson-limited sky-subtraction (down to  $i=21.5$ ) by assigning holes to monitor the sky spectrum; longer slitlets simply waste valuable CCD real-estate in regions of high target density. The fibre-hole diameters were milled at  $0''.7$  to match the median seeing. The dataset presented in this paper is the sum of all the ‘standard mask’ spectra plus ‘fibre-holes’ spectra obtained up to September 2004 that do not use the band-limiting filter. A total of 28 fields were observed in this way. The layout of these spectroscopic fields is displayed in Figure 4: the 5 fields D1–D5 probe the M31 disk, the 16 fields F1–F16 probe both the halo and what we

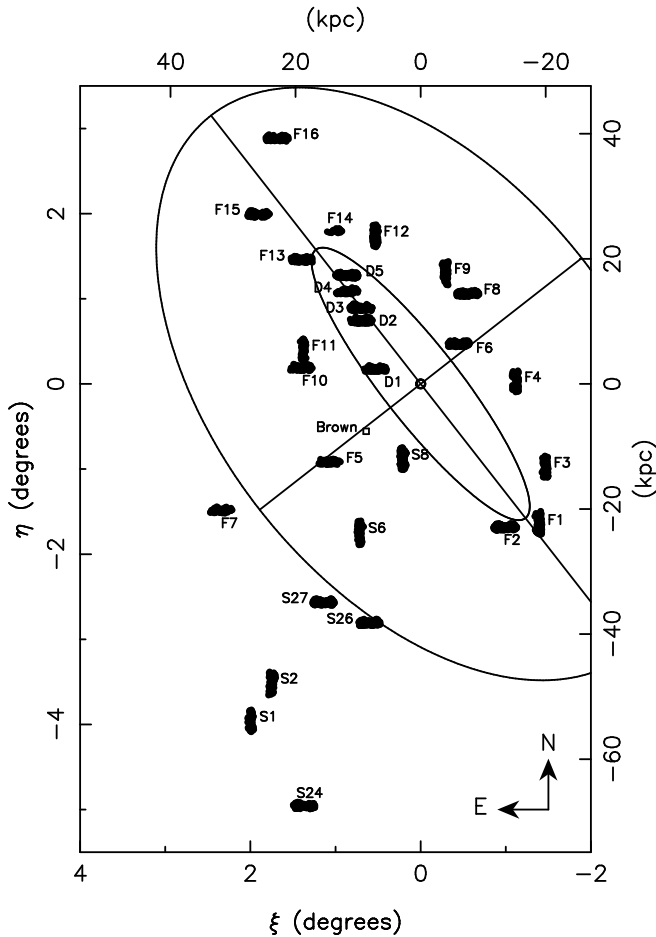


FIG. 4.— The distribution of Keck/DEIMOS fields in relation to the survey region depicted in Figure 1. For clarity, we have divided these fields into three groups. The fields in the giant stream are prefixed by the letter S, and we keep the same field names as in Ibata *et al.* (2004), with the addition of fields S24, S26, and S27. Those fields located within the inner ellipse are denoted D1–D5. The remaining fields are named F1–F16. The small square labeled “Brown” on the South-eastern minor axis marks the location of the deep photometric study of Brown *et al.* (2003), whose relevance to the present work we discuss in §6.

considered to be “halo” overdensities, while 7 fields were assigned to investigate the dynamics of the giant stream (Ibata *et al.* 2001b) which is seen clearly in Figure 1 as an elongated structure to the South-east of M31.

For each of these fields except the stream fields, the highest priority targets were selected for observation from the INT survey within a color-magnitude box with I-band magnitudes between  $20.5 < i < 22.0$  (without reddening correction) and colors  $1.0 < (V - i)_0 < 4.0$ . This broad selection was designed to pick out a wide range of red-giant branch stars, containing both metal-poor and metal-rich populations (further details will be provided in Irwin *et al.* 2005, in prep). Other non-saturated targets brighter than  $i = 22$  were also chosen by an automated selection algorithm at lower priority to fill in available space on the spectrograph detector.

Each mask was observed for typically three integrations of 20 min each. The spectroscopic images were processed and combined using the pipeline software de-

veloped by our group. This software debiases, performs a flat-field, extracts, wavelength-calibrates and sky-subtracts the spectra. The radial velocities were measured by cross-correlating against a model template with Gaussian functions at the rest-frame wavelength positions of the Ca II triplet lines (the technique used is similar to that discussed by Wilkinson *et al.* 2004). An estimate of the radial velocity uncertainty is then obtained from the dispersion of the radial velocity measured from the three Ca II triplet lines separately. The accuracy of these data are very good for such faint stars, with typical uncertainties of  $5\text{--}10 \text{ km s}^{-1}$ . The sample presented in this paper consists of 2834 stars with velocity uncertainties  $< 20 \text{ km s}^{-1}$  that fall into the above RGB color-magnitude selection window.

#### 4. RESULTS

The velocity distribution of all the targeted stars with  $(V - i)_0 > 1.0$  is displayed on the top panel of Figure 5. This distribution is a mixture of bona-fide M31 stars plus a contamination from Galactic stars. We have superimposed the expected Galactic contribution over a  $0.25^\circ$  area in the direction of M31 according to the Besançon Galactic starcounts model (Robin *et al.* 2004), onto which we have applied the color-magnitude selection window used for spectroscopic target selection. Since we have not observed every star in each field, and since the ratio of M31 to Milky Way stars varies dramatically from the inner fields to the outer fields, we cannot easily scale the model predictions. For the illustrative purposes of Figure 5, we have chosen a normalization to match the Besançon model to our observed distribution for velocities higher than the peak in the model. We will return to the issue of Galactic contamination in our analysis of field F16 (Figure 24), placing an upper limit on the model normalisation, which shows that Galactic contamination is low at Heliocentric radial velocities below  $-100 \text{ km s}^{-1}$ . It is clear from a visual comparison of the distributions in Figure 5 that we observe a large number of stars in significant excess over the expected distribution of contaminants. The apparent mismatch between the peak in the observed distribution and the Besançon model is due to the large number of stars observed in the disk fields D1–D5 on the North-eastern side of Andromeda, which combine in this summed-up plot to give a broader peak centered on  $-60 \text{ km s}^{-1}$ . If we instead sum up the 11 fields on the South-western side of M31 (fields F1–F4 and all the stream fields), the rotation of the M31 disk separates Galactic stars from the majority of stars in Andromeda, allowing a cleaner discrimination. This is shown on the bottom panel of Figure 5. These considerations show that by selecting stars with velocities  $< -100 \text{ km s}^{-1}$  we can drastically minimize the Galactic contamination, incurring only the penalty of including a small fraction of Galactic halo stars into our sample; furthermore these Galactic halo stars are expected to have a relatively flat distribution in radial velocity.

Due to the wide coverage of the spectroscopic fields, it is useful to compare the observed velocity of a star with the expected radial velocity of a population moving in circular orbits. We construct a simple model assuming the geometrical model discussed in §2. We adopt the circular velocity curve compilation of Klypin, Zhao & Somerville (2002), which joins CO measurements from

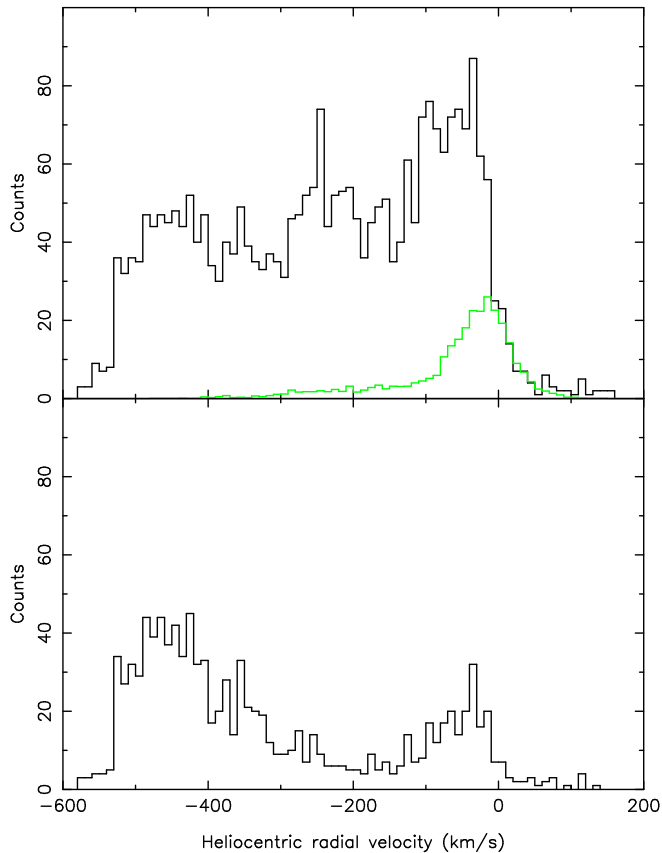


FIG. 5.— The top panel shows the velocity distribution of the 2834 RGB star candidates in all fields shown in Figure 4 that pass our color-magnitude and spectrum quality criteria. The green-lined histogram shows the prediction of the Besançon Galactic model for an area of 240 sq. arcmin within our color-magnitude selection window. With this normalization, the model fits the high-velocity edge of the observed velocity distribution. The bottom panel shows the summed distribution of stars in the fields F1–F4 plus all the stream fields.

Loinard, Allen & Lequeux (1995) for  $R < 10$  kpc with H I measurements by Brinks & Burton (1984) at larger radii; these data are reproduced in Figure 6, along with our spline fit which is shown adjusted for the small inclination correction. The dip in the rotation curve near 5 kpc is of course an artifact of non-circular motions in the gas at that location, and is unimportant for the present work since our fields all lie beyond that radius. The corresponding map of the projected rotation velocity over the inner region of our survey is shown in Figure 7.

In reality, the M31 disk has finite thickness, and due to the highly inclined orientation that it presents to us, lines of sight through the disk will probe a substantial depth. This is a concern as the simple circular velocity model of Figure 7 could be misleading, since stars at a given  $(\xi, \eta)$  on the sky can be located at different radii in M31, and will also present different projections to us. In Figure 8 we show the velocity uncertainty caused by a disk scale-height of 0.35 kpc, a value comparable to the scale-height of the old disk of the Milky Way (Gilmore & Reid 1983). For most of the survey area the additional uncertainty to the circular velocity model due to a disk of that thickness is less than  $10 \text{ km s}^{-1}$ , though certain regions within the

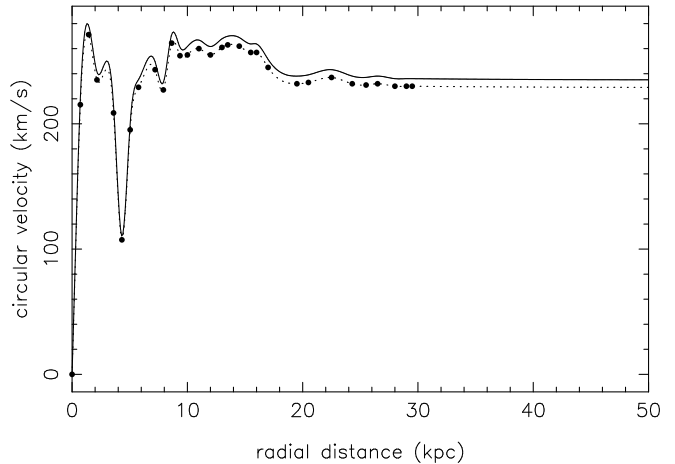


FIG. 6.— The rotation curve of M31. The points show a rotation curve compilation by Klypin, Zhao & Somerville (2002), which is derived from CO rotation velocities measurements (Loinard, Allen & Lequeux 1995) for  $R < 10$  kpc, and from the rotation velocity of the H I (Brinks & Burton 1984) beyond that radius. The dotted line shows a spline fit to these data, while the continuous line indicates the correction for the  $77^\circ$  inclination of the inner disk of this galaxy.

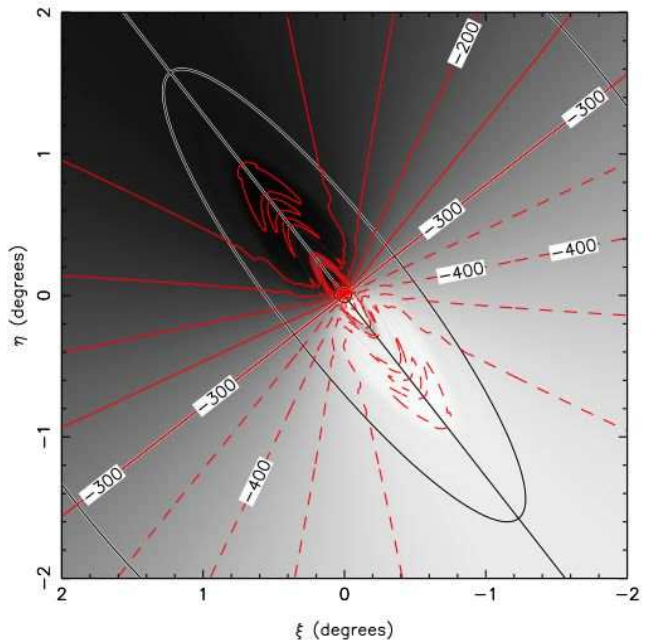


FIG. 7.— A simple model for the expected velocity of stars on circular orbits as a function of position around M31, made by projecting the spline fit of Figure 6 using the geometrical model proposed in §2. For comparison with Figures 1 and 4, we have superimposed the inner ellipse, and a section of the outer ellipse displayed in those figures onto this diagram. The radial velocity contours are shown at intervals of  $50 \text{ km s}^{-1}$ .

inner ellipse the uncertainty is  $> 30 \text{ km s}^{-1}$ . We will bear this consideration in mind when discussing the kinematic properties of the disk.

#### 4.1. Inner fields

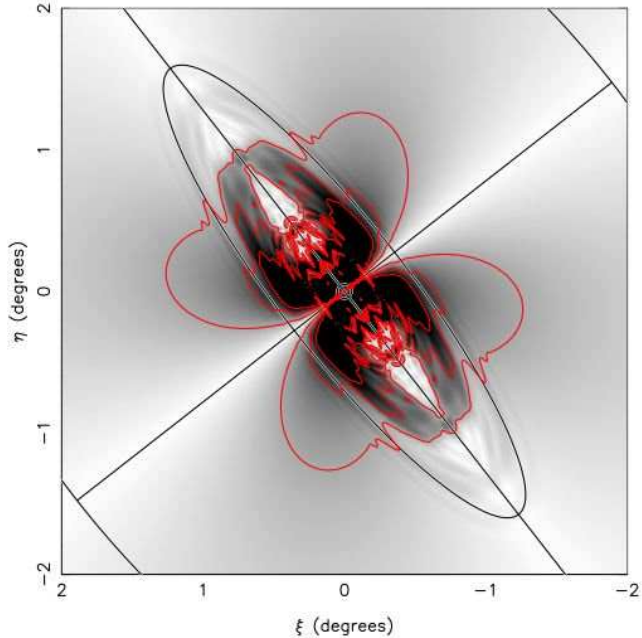


FIG. 8.— Since the Andromeda galaxy is observed close to edge-on, lines of sight through the disk can transverse a significant depth, unless the disk is infinitesimally thin. Here we illustrate the uncertainty caused by a 350 pc disk scale-height on the circular velocity predictions displayed in Figure 7. The contours show the levels where the uncertainty in the circular velocity model due to this disk thickness attains values of (from the outside in) of  $10 \text{ km s}^{-1}$ ,  $20 \text{ km s}^{-1}$  and  $30 \text{ km s}^{-1}$ . We include this additional error in when calculating the lag in velocity of stars behind the circular speed. However, over most of the survey region this additional uncertainty is less than  $10 \text{ km s}^{-1}$ .

We now proceed to present the velocity data. The upper panel of Figure 9 shows the (Heliocentric) radial velocity measurements as a function of  $x$ , the major axis distance<sup>7</sup> for the disk fields labeled D1–D5 and which lie within the inner ellipse of Figures 1 and 4 (corresponding to a disk radius  $R < 27 \text{ kpc}$ ); a small number of stars from field F13 also fall into this selection. The dashed line here marks a Heliocentric velocity of  $v = -300 \text{ km s}^{-1}$ , the adopted systemic velocity of M31. Non-rotating populations such as might be expected for the stellar halo, will scatter in a broad distribution around this line. In these North-eastern fields, the disk lies at radial velocities above the systemic value, so counter-rotating populations can be identified from their location below the dashed line. The bottom panel shows the result of subtracting the model of Figure 7 from the velocity data on a star by star basis (rather than using a single value for a whole field). Stars on circular orbits in the plane of the disk lie at a disk-corrected velocity of  $v_{lag} = 0$  (emphasized with a dashed line). Field D1 (at a major axis distance of  $x \sim 7 \text{ kpc}$ ) appears to be peculiar with an intriguing kinematic sub-structure at Heliocentric velocity of  $v \sim -250 \text{ km s}^{-1}$ ; we will discuss this structure in a subsequent contribution. It is interesting to note that this sub-structure was only detected through

<sup>7</sup> We define the major axis distance as the distance from the minor axis towards the North-east parallel to the major axis.

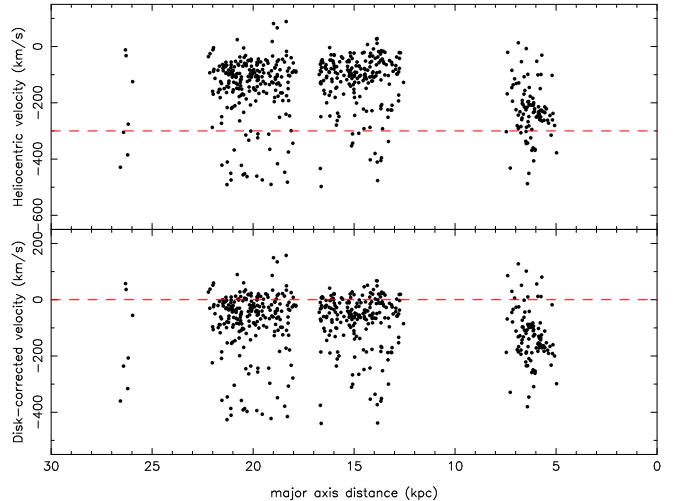


FIG. 9.— Radial velocity as a function of major axis distance for fields D1–D5 (with a few stars from F13 that lie within the inner ellipse of Figure 4). The upper panel shows the Heliocentric radial velocity of the stars, with the dashed line marking the systemic velocity of M31. The bottom panel shows the same data “corrected” for the expected disk rotation given by the model shown in Figure 7; now the dashed line marks the location of stars on circular orbits. Note the obvious structure that is present in the field at major axis distance of  $\sim 7 \text{ kpc}$  (field D1).

its kinematic signature, as there is no clear overdensity in our maps of RGB stars in this field.

However, the disk fields D2–D5 (located at major axis distances between  $12 \text{ kpc} < x < 23 \text{ kpc}$ ) show a very similar distribution of stars, with a broad halo component below  $v_{lag} = -150 \text{ km s}^{-1}$ , and a well-populated peak lagging circular orbits only slightly. In Figure 10 we show the distribution of disk lag velocities for fields D2–D5, together with a Gaussian fit of the data between  $-150 \text{ km s}^{-1} < v_{lag} < 100 \text{ km s}^{-1}$ , which has a mean of  $\bar{v}_{lag} = -34 \text{ km s}^{-1}$  with dispersion of  $\sigma_v = 47 \text{ km s}^{-1}$  ( $\bar{v}'_{lag} = -18 \text{ km s}^{-1}$ ,  $\sigma_{v'} = 47 \text{ km s}^{-1}$ ). The dash-dotted line shows a similar maximum-likelihood Gaussian fit, this time taking into account the estimated velocity uncertainty on the individual velocity measurements, and also the uncertainty in the disk rotation model (from Figure 8). This fit, which has  $\bar{v}_{lag} = -37 \text{ km s}^{-1}$  and  $\sigma_v = 44 \text{ km s}^{-1}$  ( $\bar{v}'_{lag} = -23 \text{ km s}^{-1}$ ,  $\sigma_{v'} = 45 \text{ km s}^{-1}$ ), shows that the dispersion of the population is not artificially enhanced to any significant extent by our line of sight depth through these fields.

As discussed above, contamination from Milky Way stars can be problematic for  $v > -100 \text{ km s}^{-1}$ ; however the M31 disk has very high contrast in these inner fields (D1–D5), with a source surface density in our CMD selection window that is 20 times higher than in the halo field F7, so we expect the Galactic contamination to be small, 5% at the very most. Thus we find that the dominant population in the inner regions of M31 is a thin disk population with a dispersion of  $\sigma_v = 44 \text{ km s}^{-1}$  that trails circular orbits by  $\bar{v}_{lag} = -37 \text{ km s}^{-1}$ ; these values are reasonably similar to the measurements of the velocity dispersion of the Galactic disk in the Solar Neighborhood where the velocity ellipsoid has axes

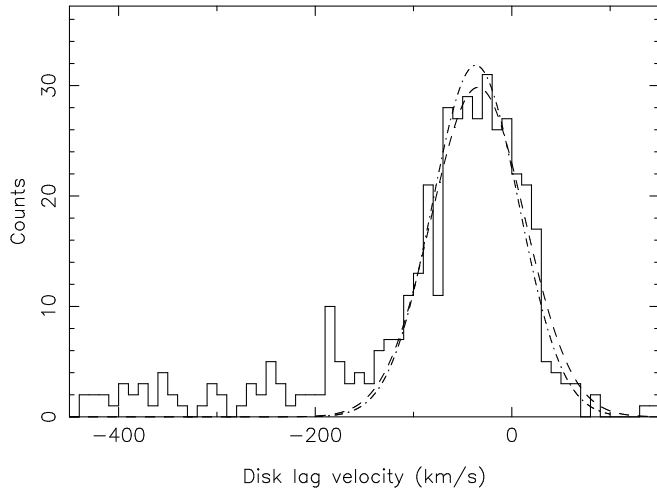


FIG. 10.— The summed distribution of velocity lags of fields D2–D5 (i.e. stars with major axis distances between 12 kpc to 23 kpc in Figure 9). The large peak between  $-150 \text{ km s}^{-1} < v_{lag} < 100 \text{ km s}^{-1}$  can be fit with a Gaussian (dashed line) of mean  $\bar{v}_{lag} = -34 \text{ km s}^{-1}$  and dispersion  $\sigma_v = 47 \text{ km s}^{-1}$  ( $\overline{v'}_{lag} = -18 \text{ km s}^{-1}$ ,  $\sigma_{v'} = 47 \text{ km s}^{-1}$ ). The fit does not change significantly if we take into account the estimated velocity errors and the disk rotation model uncertainties displayed in Figure 8, we obtain then (dot-dashed line)  $\bar{v}_{lag} = -37 \text{ km s}^{-1}$ ,  $\sigma_v = 44 \text{ km s}^{-1}$  ( $\overline{v'}_{lag} = -23 \text{ km s}^{-1}$ ,  $\sigma_{v'} = 45 \text{ km s}^{-1}$ ).

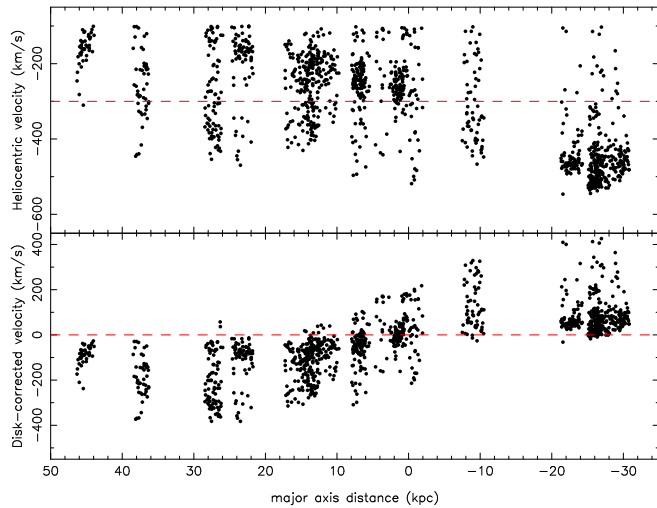


FIG. 11.— As Figure 9, but for the 16 fields F1–F16 that lie outside of the inner ellipse shown in Figures 1 and 4, and which do not lie in the giant stream. In most of these fields the dominant population of stars is seen with velocities lagging the circular velocity by velocities between  $0 \text{ km s}^{-1}$  to  $\sim 100 \text{ km s}^{-1}$ .

$(\sigma_R, \sigma_\phi, \sigma_z) = (38 : 24 : 17) \text{ km s}^{-1}$  and the population lags the circular velocity with an asymmetric drift of  $\sim 20 \text{ km s}^{-1}$  (Dehnen & Binney 1998). The asymmetric drift of the M31 population will be discussed further in §6.1. Note that the very inclined orientation of M31 means that we do not have access to the vertical dispersion  $\sigma_z$ . The measured  $\sigma_v$  is a mixture of the radial and azimuthal components  $\sigma_R$  and  $\sigma_\phi$ , dependent on the field under study. For simplicity we neglect this distinction in the present discussion, referring to a single  $\sigma_v$ .

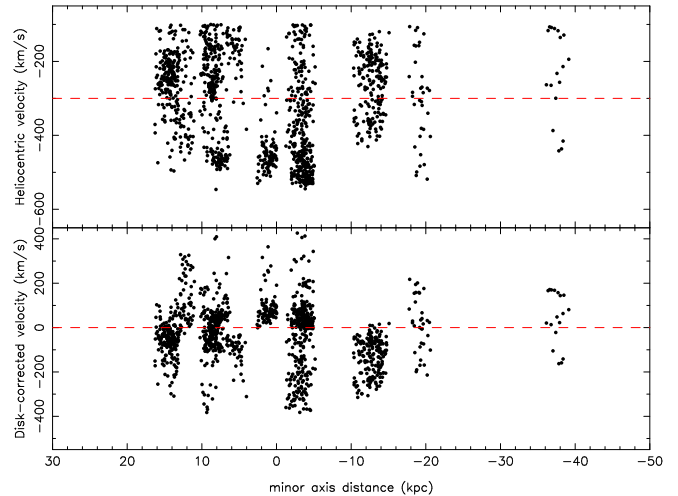


FIG. 12.— As Figure 11, but showing the velocity as a function of minor axis distance.

#### 4.2. Outer fields

Having shown that the inner fields have kinematics typical of a canonical thin disk, we now examine the outer field data. The fields lying on the giant stellar stream (those prefixed by the letter ‘S’ in Figure 4) are removed from the sample for the sake of simplicity. This leaves a total of 16 fields marked F1–F16 on Figure 4.

The measured radial velocities in these fields are displayed as a function of major axis distance on the top panel of Figure 11. For clarity, we have removed from this sample all stars with heliocentric velocities  $v > -100 \text{ km s}^{-1}$ , thereby minimizing the Galactic contamination (*cf.* Galactic model in Figure 5). There is a wealth of kinematic substructure in these fields (Chapman *et al.* 2005, in prep), and a significant halo population seen scattered around the systemic velocity (dashed line); however the dominant population in these fields again follows closely the disk rotation. This can be seen on the bottom panel of Figure 11, where we have corrected the data on the upper panel for the rotation model of Figure 7. In the fields at major axis distance between  $-20 \text{ kpc} < x < -30 \text{ kpc}$ , the numerous population stands out clearly with “disk-corrected velocity” between  $0 \text{ km s}^{-1}$  and  $100 \text{ km s}^{-1}$ . On this South-western side of M31, these velocities correspond to a lagging behind the H I. On the opposite side of the disk, at major axis distances  $x > 5 \text{ kpc}$ , a similar concentration is found with “disk-corrected velocity” between  $-100 \text{ km s}^{-1}$  and  $0 \text{ km s}^{-1}$ , this again corresponds to a lagging velocity behind the H I gas.

For completeness, in Figure 12 we show the same velocity data as a function of minor axis distance<sup>8</sup>,  $y$ . It is clear from this diagram that the halo fields F5 and F7 (the two fields at minor axis distance  $y < -15 \text{ kpc}$ ) do not contribute significantly (if at all) to the peaked velocity structure that rotates as a disk.

Figure 13 shows the distribution of velocity lag  $v_{lag}$  in the 16 fields under consideration. The velocity lag is de-

<sup>8</sup> We define the minor axis distance as the distance from the major axis towards the North-west parallel to the minor axis.

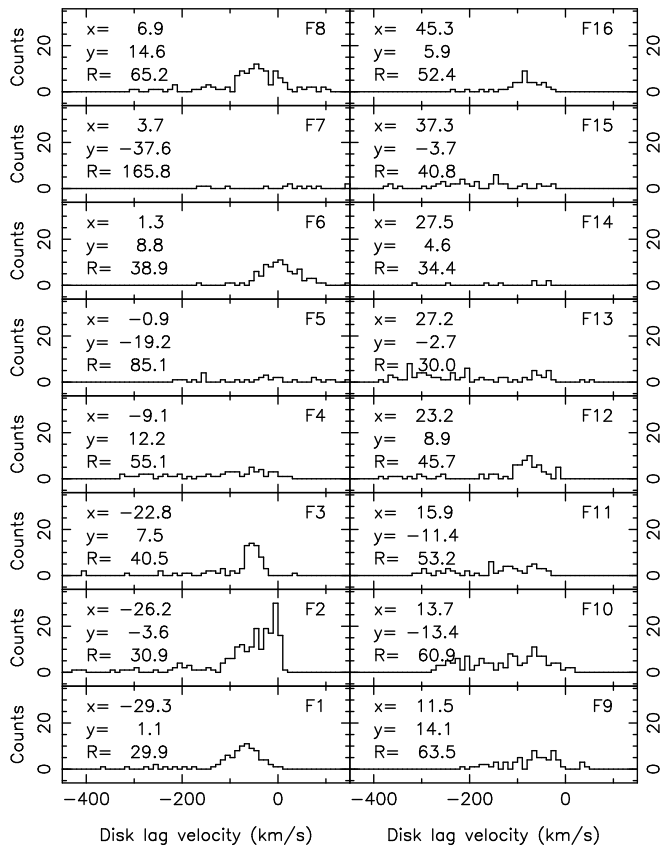


FIG. 13.— Distributions of the velocity lag behind the circular velocity model for the 16 fields displayed in Figure 11. In each panel the three numbers show, respectively, from top to bottom, the major axis distance, the minor axis distance, and the de-projected radius  $R$  of the fields. The field name is also indicated.

finned to be equal to the disk-corrected velocity for fields at positive major axis distance, but is inverted for fields at negative major axis distance. Each panel is labeled with the field name and as well as three numbers which give the major axis distance  $x$ , the minor axis distance  $y$  and the de-projected M31-plane radius  $R$ , of the centre of each field, all in kpc. A striking feature of these distributions is the presence of a narrow component in most of the fields, which lags the circular velocity by merely  $\sim 50 \text{ km s}^{-1}$ , that is to say a population which has distinctly disk-like kinematics. Yet this is a startling finding, since these fields are extremely distant from M31, lying at radial distances between 30 kpc and more than 50 kpc. That this behavior is the most salient kinematic feature of the survey is demonstrated in Figure 14, which shows the distribution of velocity lag as a function of the M31-plane radial distance,  $R$ , for all stars in the survey in non-stream fields with  $R < 80 \text{ kpc}$ . The majority of the stars are found with disk lag velocity in the range  $-100 \text{ km s}^{-1} < v_{lag} < 0 \text{ km s}^{-1}$ , and therefore take part in a large-scale rotational motion.

Summing the velocity lag distributions in all the outer non-stream fields (except for F6 to remove any concern regarding contamination from NGC 205 — this will be discussed further in §5.4) gives the distribution shown in Figure 15. This distribution is very similar to that previously constructed for the inner fields (*cf.* Figure 10),

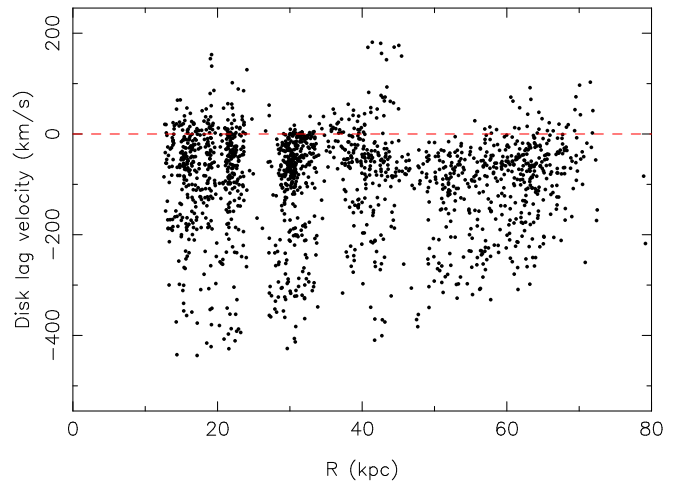


FIG. 14.— The distribution of velocity lags as a function of M31-plane de-projected radial distance in all non-stream survey fields at  $R < 80 \text{ kpc}$ . The majority of these stars display small velocity lags ( $-100 \text{ km s}^{-1} < v_{lag} < 0 \text{ km s}^{-1}$ ), and are therefore rotating rapidly. The dashed line shows the location of circularly-rotating stars.

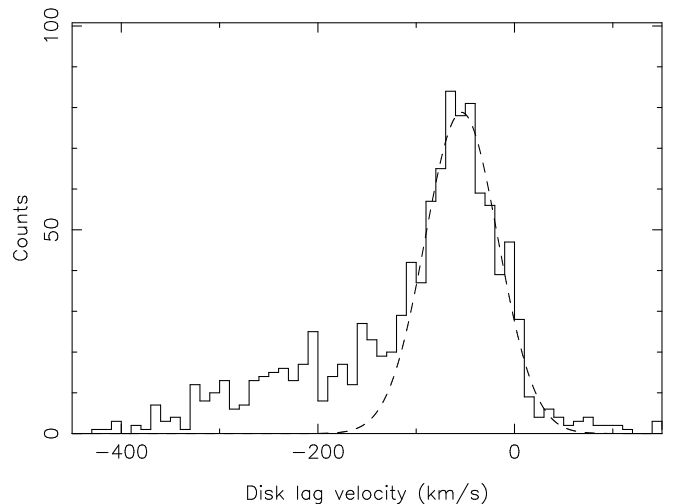


FIG. 15.— The summed distribution of velocity lags in all fields in Figure 13, except F6. A Gaussian fit to the data between  $-150 \text{ km s}^{-1} < v_{lag} < 100 \text{ km s}^{-1}$  is superimposed (dashed line), which has mean at  $\bar{v}_{lag} = -54 \text{ km s}^{-1}$  and a dispersion of  $\sigma_v = 37 \text{ km s}^{-1}$  ( $\bar{v}'_{lag} = -41 \text{ km s}^{-1}$ ,  $\sigma_{v'} = 38 \text{ km s}^{-1}$ ).

showing again a broad halo distribution with the addition of a very strong peak, in this case centered at  $\bar{v}_{lag} = -54 \text{ km s}^{-1}$  with a dispersion of  $\sigma_v = 37 \text{ km s}^{-1}$  ( $\bar{v}'_{lag} = -41 \text{ km s}^{-1}$ ,  $\sigma_{v'} = 38 \text{ km s}^{-1}$ ).

These data unambiguously show that the bulk of the stars in our survey fields share a common kinematic property: they co-rotate with the H I gas, with velocities that lag that of the gas by  $\sim 40 \text{ km s}^{-1}$ , and possess a velocity dispersion of  $\sim 40 \text{ km s}^{-1}$ . There therefore appears to be a vast stellar disk-like structure around the Andromeda galaxy, distributed on an unprecedented scale.

## 5. OVERVIEW OF SELECTED OUTER FIELDS

We next present in detail the data from 7 of the outer fields, selected from Figure 13 for having a particularly

strong disk-like peak in their velocity distributions. The selected fields are F1, F2, F3, F6, F8, F12 and F16.

### 5.1. Field F1

Field F1 lies at the South-western boundary of the conspicuous dark and messy structure in Figure 1 that surrounds the bright inner disk seen in photographic surveys. The most massive of the M31 outer globular clusters, named “G1” also lies in this field, and we refer to the structure at this location as the G1 clump. We summarize the structural, kinematic and photometric data on this field in Figure 16. The upper left-hand panel gives the location of the field with respect to the large survey area, which we zoom into in the upper right hand panel. The bottom left panel shows the velocity distribution of the stars in our RGB selection window, together with a Gaussian fit centered at  $\bar{v}_{lag} = -69 \text{ km s}^{-1}$  with dispersion  $\sigma_v = 30 \text{ km s}^{-1}$  ( $\bar{v}'_{lag} = -51 \text{ km s}^{-1}$ ,  $\sigma_{v'} = 29 \text{ km s}^{-1}$ ). The bottom right-hand panel shows the CMD derived from the INT survey over the  $16.7' \times 5'$  field of view of the DEIMOS instrument. Those stars with velocities within  $2\sigma$  of the mean of the Gaussian fit are marked with a filled circle. The four curves superimposed on this CMD are globular cluster fiducials, with metallicities, from left to right of  $[\text{Fe}/\text{H}] = -1.91$ ,  $[\text{Fe}/\text{H}] = -1.29$ ,  $[\text{Fe}/\text{H}] = -0.71$  and  $[\text{Fe}/\text{H}] = -0.2$ . The stars that partake in the strong peak evidently scatter in a wide distribution around  $[\text{Fe}/\text{H}] \sim -0.7$ . Both the kinematics and the spectroscopic metallicity (presented in §5.9) that we derive in this field are in excellent agreement with the findings of Reitzel, Guhathakurta & Rich (2004).

The spatial structure of this grouping of stars is very interesting. An inspection of the top right-hand panel (and also Figure 1) shows that this structure is an irregular lump – somewhat elongated E-W and apparently distinct from the disk. The structure is very large, being more than 10 kpc long. It is highly unlikely that this structure is bound, as this would require some  $\sim 10^9 M_\odot$  of dark matter, given the velocity dispersion and extent. Instead, the disorderly morphology argues in favor of this being tidal debris.

### 5.2. Field F2

Field F2 (Figure 17) is located close to Field F1, but in a prominence that descends southwards of the disk. The velocity distribution in field F2 is similar to that of Field F1, but contains an additional narrow component, which is seen as a spike near  $v_{lag} = 0$  in the bottom left hand panel of Figure 17. Fitting two Gaussian functions yields a narrow peak at  $\bar{v}_{lag} = -4 \text{ km s}^{-1}$  with dispersion  $\sigma_v = 7 \text{ km s}^{-1}$  ( $\bar{v}'_{lag} = 11 \text{ km s}^{-1}$ ,  $\sigma_{v'} = 5 \text{ km s}^{-1}$ ), and a broader peak with  $\bar{v}_{lag} = -46 \text{ km s}^{-1}$  and  $\sigma_v = 35 \text{ km s}^{-1}$  ( $\bar{v}'_{lag} = -29 \text{ km s}^{-1}$ ,  $\sigma_{v'} = 33 \text{ km s}^{-1}$ ). The stars that gives rise to the narrow kinematic spike are dispersed spatially over the whole DEIMOS field, so the structure is not simply a cluster. The small velocity dispersion and the mean velocity almost exactly on the expected circular rotation imply that the the population is almost certainly young. The population in the broad kinematic peak is again very similar to the peak that we observe in field F1 and in the inner fields D2–D5.

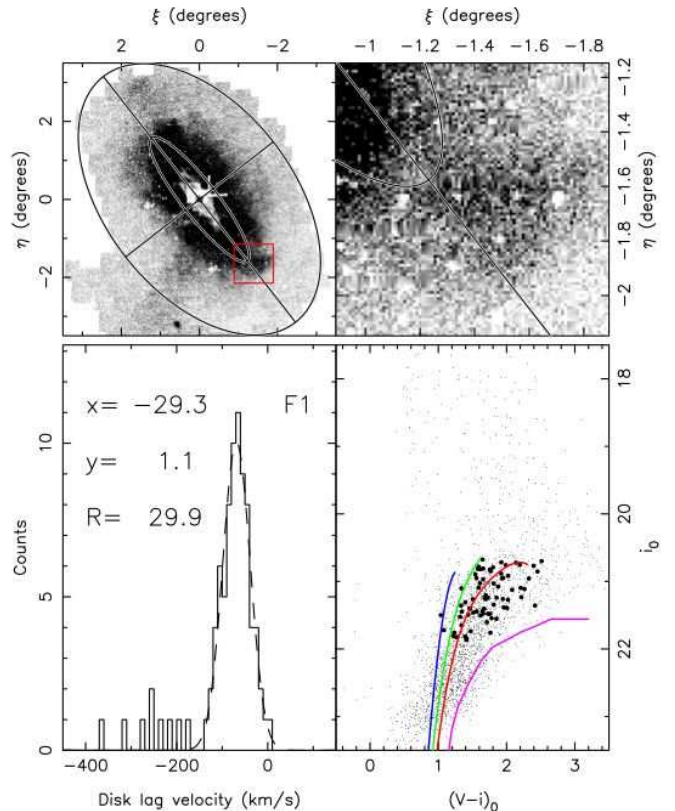


FIG. 16.— The upper left panel shows the location of the field F1 in our survey region (compare to Figure 1), with a  $1^\circ \times 1^\circ$  box marking the location of the zoomed-in view displayed on the right-hand panel, which is centered on the centre of this DEIMOS field. The white holes present in this map are due to the halos of bright stars. The bottom left-hand panel shows the distribution of the velocity lag behind the circular velocity in this field, together with a single-component Gaussian fit, which has a mean of  $\bar{v}_{lag} = -69 \text{ km s}^{-1}$  and dispersion of  $\sigma_v = 30 \text{ km s}^{-1}$  ( $\bar{v}'_{lag} = -51 \text{ km s}^{-1}$ ,  $\sigma_{v'} = 29 \text{ km s}^{-1}$ ). The bottom-right panel shows the color-magnitude diagram of the field, with small dots showing the full INT photometry within the area of the DEIMOS field of view. The filled circles are the stars with observed velocities within  $\pm 2\sigma$  of the fitted Gaussian on the bottom left-panel. For comparison, we have superimposed fiducial cluster sequences for (from left to right) NGC 6397, NGC 1851, 47 Tuc and NGC 6553, which have metallicities of  $[\text{Fe}/\text{H}] = -1.91$ ,  $[\text{Fe}/\text{H}] = -1.29$ ,  $[\text{Fe}/\text{H}] = -0.71$  and  $[\text{Fe}/\text{H}] = -0.2$ , respectively.

### 5.3. Field F3

Field F3 is located towards the South-west of M31, on a dense elongated structure that trails behind the disk in a way that is reminiscent of a tidal stream or the end of a spiral arm (see Figure 18). Though the velocity dispersion of  $\sigma_v = 15 \text{ km s}^{-1}$  is relatively low in this field, the color-magnitude position of the stars that populate the kinematic peak is very similar to that seen in other fields.

### 5.4. Field F6

Figure 19 shows the velocity and color-magnitude data for field F6, centered on the Northern edge of NGC 205, one of the dwarf elliptical satellite galaxies of Andromeda. The distribution of velocities has a narrow peak centered at  $\bar{v}_{lag} = 2 \text{ km s}^{-1}$  with dispersion  $\sigma_v = 36 \text{ km s}^{-1}$  ( $\bar{v}'_{lag} = 4 \text{ km s}^{-1}$ ,  $\sigma_{v'} = 37 \text{ km s}^{-1}$ ). Sur-

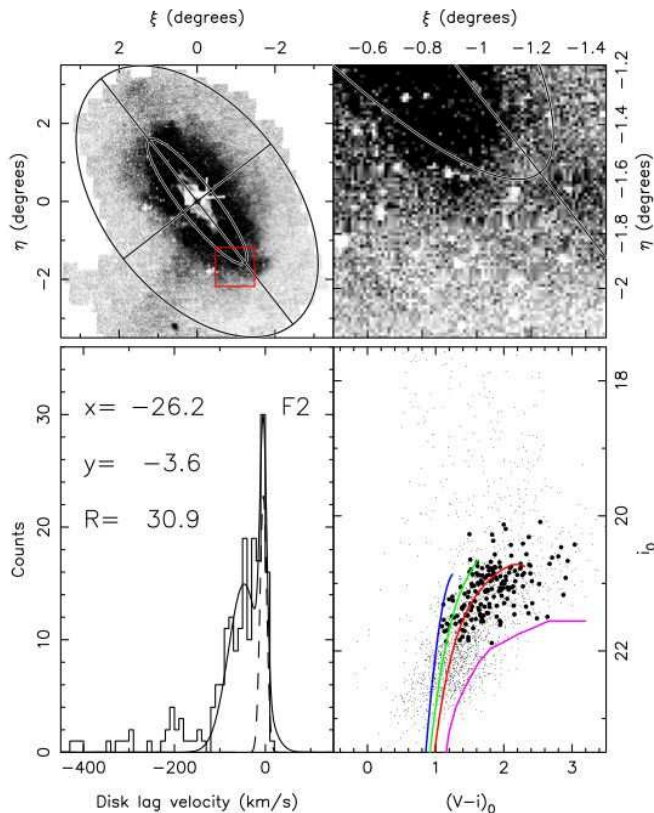


FIG. 17.— As Figure 16, but for field F2. In this case we have fit a two-component Gaussian model: we find a narrow peak centered at  $\bar{v}_{lag} = -4 \text{ km s}^{-1}$  with dispersion of  $\sigma_v = 7 \text{ km s}^{-1}$  ( $\bar{v}'_{lag} = 11 \text{ km s}^{-1}$ ,  $\sigma_{v'} = 5 \text{ km s}^{-1}$ ), and a broader peak with  $\bar{v}_{lag} = -46 \text{ km s}^{-1}$  and  $\sigma_v = 35 \text{ km s}^{-1}$  ( $\bar{v}'_{lag} = -29 \text{ km s}^{-1}$ ,  $\sigma_{v'} = 33 \text{ km s}^{-1}$ ).

prisingly, this distribution is very similar to what has been found previously in other fields: the velocity dispersion is small and consistent with a circularly rotating population. Figure 20 displays the velocity and spatial data in more detail, with the middle panel showing the target positions with respect to a sketch of NGC 205. The upper panel gives the heliocentric velocity measurements, while the bottom panel shows the velocity lag as a function of standard coordinate  $\xi$ . It is interesting to note that if some stars in this field were being removed from NGC 205 by the action of tidal forces, they would contribute, at least in projection, to stars with disk-like kinematics; we return to this point in §6 below.

### 5.5. Field F8

Figure 21 shows the data for field F8, a field in the possible tidal trail of NGC 205. This structure was discussed previously by McConnachie et al. (2004b), where they presented the morphology of the feature, together with kinematics from our field F9 (their field W91). The new data in field F8 (adjacent to field F9) do not show the bimodal distribution found by McConnachie et al. (2004b), which suffered from a small sample size. Instead the only significant stellar population present has, yet again, disk-like kinematics with a dispersion of  $\sigma_v = 38 \text{ km s}^{-1}$  centered at  $\bar{v}_{lag} = -43 \text{ km s}^{-1}$  ( $\bar{v}'_{lag} = -37 \text{ km s}^{-1}$ ,

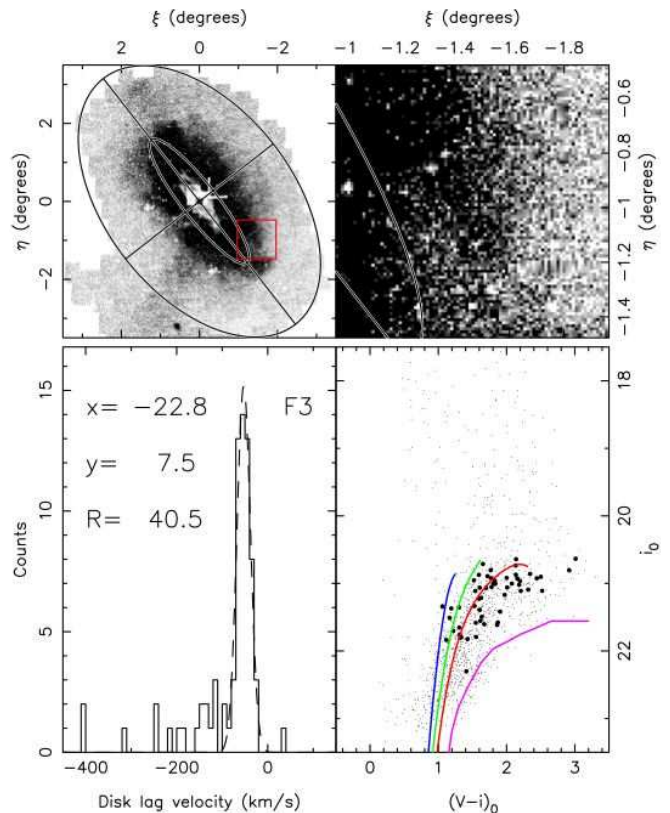


FIG. 18.— As Figure 16, but for field F3. The Gaussian model has  $\bar{v}_{lag} = -53 \text{ km s}^{-1}$  and  $\sigma_v = 15 \text{ km s}^{-1}$  ( $\bar{v}'_{lag} = -37 \text{ km s}^{-1}$ ,  $\sigma_{v'} = 15 \text{ km s}^{-1}$ ).

$\sigma_{v'} = 35 \text{ km s}^{-1}$ ).

### 5.6. Field F12

Figure 22 shows the location of another dense structure, this time located towards the North-eastern end of the major axis. A peculiarity of this feature (the “Northern Spur”) is its curious wedge-shaped morphology (seen in the upper right-hand diagram) which displays a very sharp boundary. The velocity dispersion of the structure  $\sigma_v = 24 \text{ km s}^{-1}$  ( $\sigma_{v'} = 23 \text{ km s}^{-1}$ ) is again similar to that in other fields.

### 5.7. Field F16

Field F16 is situated in a particularly interesting location, on the North-eastern end of our survey region (see Figure 23), where our INT survey detected a very extended very low surface brightness structure. It lies at the greatest projected radius (46 kpc) of all the non-stream fields we observed. Zucker et al. (2004) argue that this object (which they call Andromeda NE) may be one of the most low mass and low surface brightness galaxies found to date or possibly torn-off material from the disk of M31. The radial velocity distribution in the bottom left-hand panel of Figure 23 shows a well-defined narrow peak of dispersion  $\sigma_v = 27 \text{ km s}^{-1}$  centered at  $\bar{v}_{lag} = -80 \text{ km s}^{-1}$  ( $\bar{v}'_{lag} = -65 \text{ km s}^{-1}$ ,  $\sigma_{v'} = 28 \text{ km s}^{-1}$ ). However, this field is the only one in our survey in which there could be some concern about Galactic contamination affecting significantly the fitted

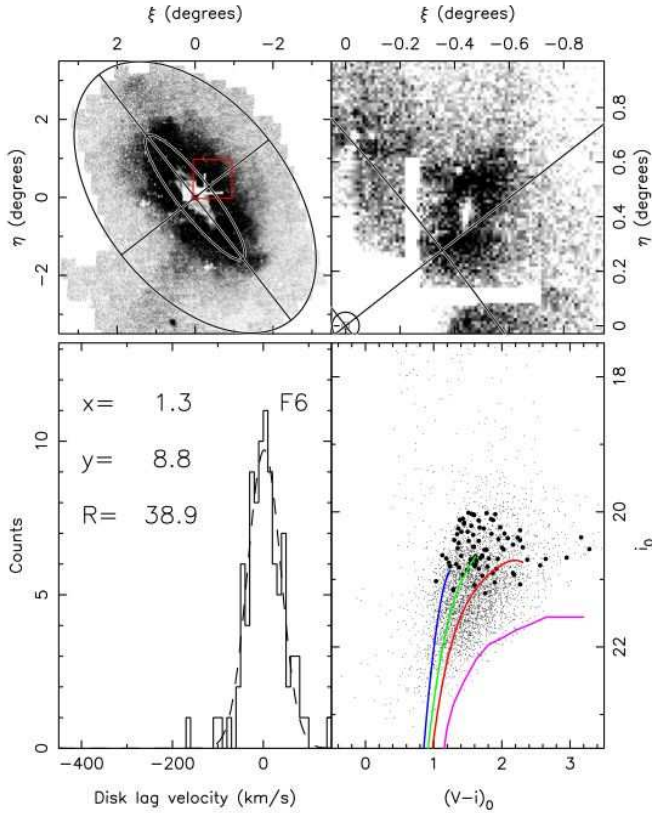


FIG. 19.— As Figure 16, but for field F6. The Gaussian model has  $\bar{v}_{lag} = 2 \text{ km s}^{-1}$  and  $\sigma_v = 36 \text{ km s}^{-1}$  ( $\bar{v}'_{lag} = 4 \text{ km s}^{-1}$ ,  $\sigma_{v'} = 37 \text{ km s}^{-1}$ ). The white “L”-shaped hole in the finding chart is due to a deliberate shifting of the camera position to centre one of the CCDs of the mosaic on NGC 205; part of the inner survey region was thereby not covered. The hole in the centre of NGC 205 is a consequence of crowding.

disk-like peak. In Figure 24 we show the Heliocentric velocity distribution of stars in this field, with the cut at  $v = -100 \text{ km s}^{-1}$ , imposed on all fields to minimize the Galactic contaminants. The predictions of the Besançon Galaxy model are superposed (green histogram) normalised to the  $16.7' \times 5'$  field of view of DEIMOS, but corrected for the ratio of available to observed targets in our CMD selection window. Thus according to this model, below  $v = -100 \text{ km s}^{-1}$  the Galactic contribution will be minor, and can be neglected. The bottom right-hand panel of Figure 23 shows the CMD location of the stars within the peak; evidently these are relatively metal-rich, and very similar to the other disk-like stars found in the fields examined previously.

The velocity histogram in the bottom left-hand panel of Figure 23 shows a spike at velocities  $-90 \text{ km s}^{-1} < v_{lag} < -80 \text{ km s}^{-1}$ . The stars partaking in this spike are uniformly distributed over the field, and they have a similar color spread to the other stars in the sample (the corresponding points are circled in the CMD on the bottom right-hand panel). This lack of distinct properties, together with the low statistics indicate that this spike is most probably an insignificant ( $\sim 2\sigma$ ) random deviation.

#### 5.8. Fields F4, F5, F7, F9, F10, F11, F13, F14 and F15

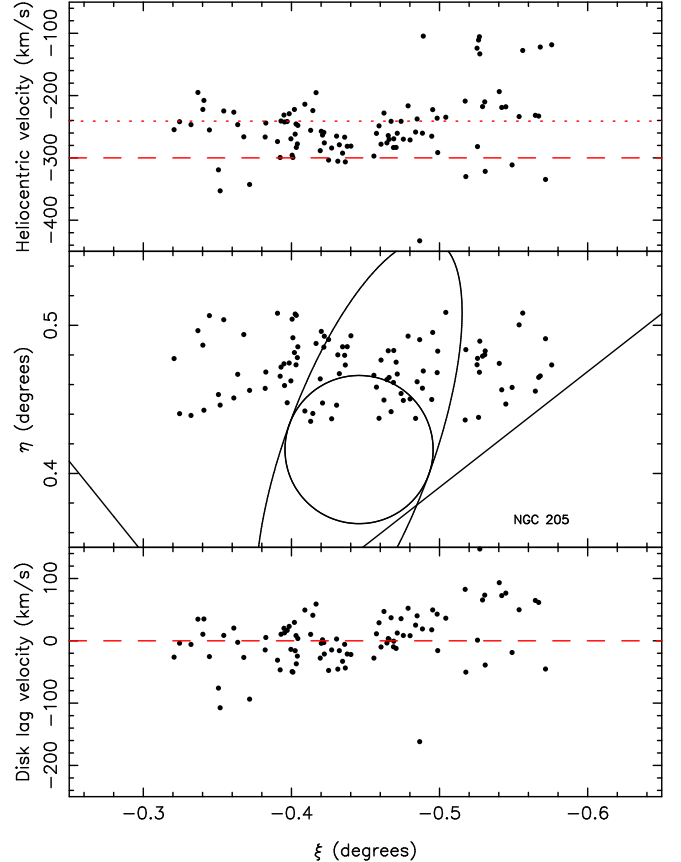


FIG. 20.— The central panel shows the positions of the targets in field F6 with respect to a sketch of NGC 205. The diagonal line segments show the minor and major axes of M31. The top and bottom panels show the kinematic data as a function of the standard coordinate  $\xi$ . The dashed line in the top panel marks the systemic velocity of M31, while the dotted line shows the systemic velocity of NGC 205. The bottom panel displays the corresponding distribution of disk lag velocity, with the dashed line marking the locus of circular orbits.

The remaining outer non-stream fields: F4, F5, F7, F9, F10, F11, F13, F14 and F15, do not individually possess a narrow and strong velocity peak near the expected velocity of a circularly rotating population (see Figure 13). However, by summing the fields together we can enhance the signal to detect a global population which lags the disk by a similar velocity. The nine fields that were added together cover a very large area over our survey. Some fields, in particular the halo field F7, are almost certainly devoid of any disk stars, so the “disk velocity lag” is not a meaningful quantity, and will contribute only noise to the summed distribution. Nevertheless, Figure 25 shows that a narrow peak is again detected, albeit with a large population of “contaminants”, this time stemming mostly from the halo population of M31 itself. Due to the kinematic substructure in the halo population (which will be presented in a forthcoming paper, Chapman et al., in prep.) we cannot easily remove the halo “contamination” to enhance the signal of the disk-like peak. Nevertheless, to help guide the eye, we have used a maximum likelihood algorithm to fit a Gaussian function to the velocity data windowed between  $-80 \text{ km s}^{-1} < v_{lag} < 50 \text{ km s}^{-1}$ , which we find to be cen-

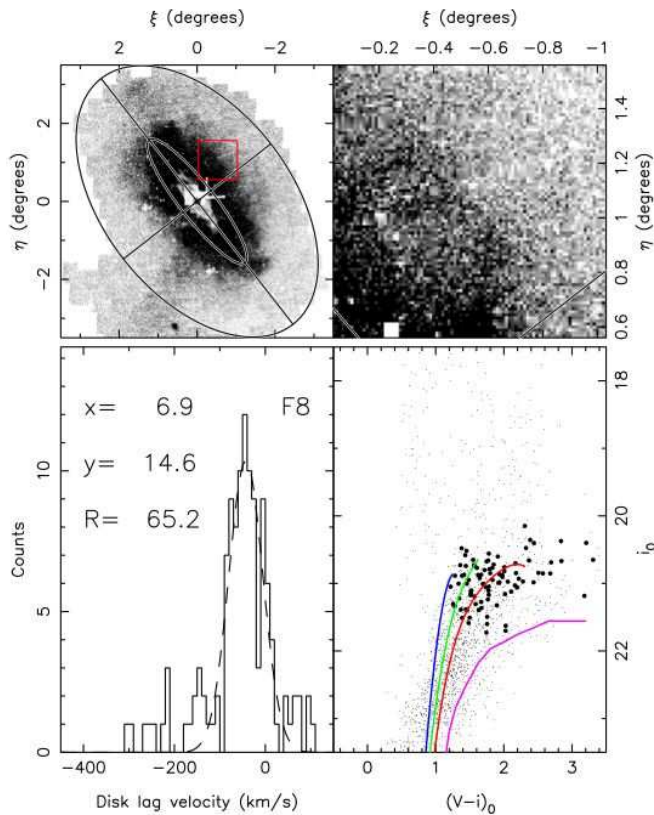


FIG. 21.— As Figure 16, but for field F8. The Gaussian model has  $\bar{v}_{lag} = -43 \text{ km s}^{-1}$  and  $\sigma_v = 38 \text{ km s}^{-1}$  ( $\bar{v}'_{lag} = -37 \text{ km s}^{-1}$ ,  $\sigma_{v'} = 35 \text{ km s}^{-1}$ ).

tered on  $\bar{v} = -55 \text{ km s}^{-1}$  with dispersion  $\sigma_v = 33 \text{ km s}^{-1}$  ( $\bar{v}'_{lag} = -41 \text{ km s}^{-1}$ ,  $\sigma_{v'} = 31 \text{ km s}^{-1}$ ). Although the reliability of this fit is clearly compromised by the strong halo contamination, the similarity of this peak with those presented in Figures 16 to 23 is very striking. This confirms that a disk-like population is present in almost all the surveyed fields.

### 5.9. Spectroscopic metallicities

The spectra also allow a measurement of the metallicity of the targeted stars from the equivalent widths (EW) of the Ca II triplet absorption lines. While the noise in individual spectra is typically too high to yield a useful measurement of the Ca II equivalent widths, we proceeded to estimate the average metallicity by stacking the RGB star spectra of the targets within  $2\sigma$  of the fitted peaks of the fields displayed in Figures 16 to 23 (the corresponding stars are also highlighted in the CMD panels). The spectra are shifted to zero velocity before stacking. We follow as closely as possible the method of Rutledge, Hesser & Stetson (1997), fitting Moffat functions to the Ca II lines. The average spectrum yields a measurement of the Ca II triplet equivalent width used to estimate the metallicity as  $[Fe/H] = -2.66 + 0.42[\Sigma Ca - 0.64(V_{HB} - V_{ave})]$ , with  $\Sigma Ca = 0.5EW_{\lambda 8498} + 1.0EW_{\lambda 8542} + 0.6EW_{\lambda 8662}$ ,  $V_{HB}$  being a surface gravity correction relative to the  $V$  magnitude of the horizontal branch, and  $V_{ave}$  the average (luminosity weighted) magnitude of the stars in the field.

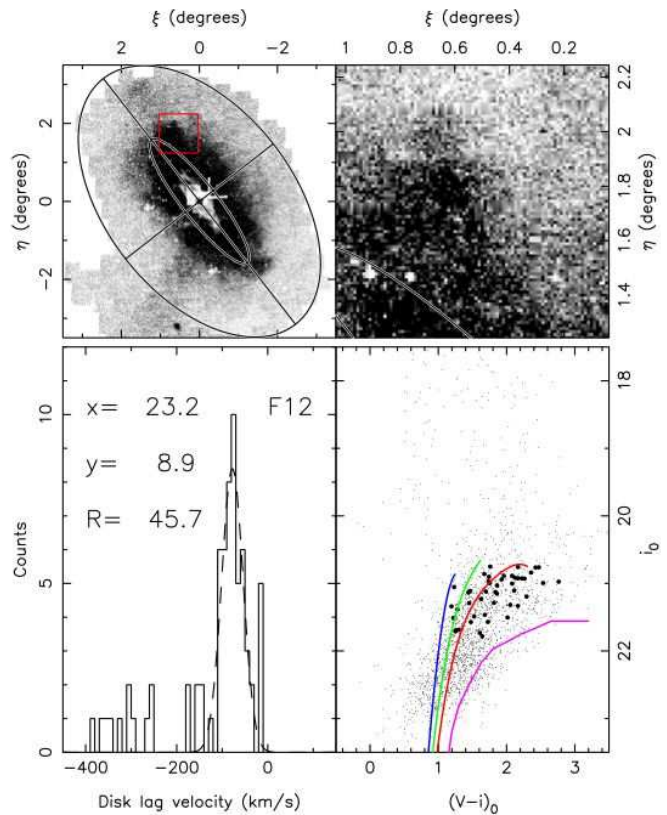


FIG. 22.— As Figure 16, but for field F12. The Gaussian model has  $\bar{v}_{lag} = -78 \text{ km s}^{-1}$  and  $\sigma_v = 24 \text{ km s}^{-1}$  ( $\bar{v}'_{lag} = -60 \text{ km s}^{-1}$ ,  $\sigma_{v'} = 23 \text{ km s}^{-1}$ ).

We adopt the value of  $V_{HB} = 25.17$  for M31, measured by Holland (1996). The resulting combined spectra are displayed in Figure 26, along with the metallicity measurement (on the Carretta & Gratton 1997 scale). The typical uncertainty is  $\sim 0.2$  mags. By chance, the  $\lambda 8498$  line in the summed spectrum in Field 16 falls at the location of a night-sky line, so the two other Ca II were used in that instance. For comparison to the inner fields, on the top panel of Figure 26 we also display the summed spectrum of the disk fields D2–D5, derived from those stars within  $2\sigma$  of the fit shown in Figure 10.

These metallicity measurements are all very similar, identical within the uncertainties, and agree reasonably well with the position of the targets relative to our fiducial clusters on the color-magnitude diagram. This yields further evidence that the dominant population in the majority of the fields we surveyed starting from the disk populations at a radius of 15 kpc out to  $\sim 50$  kpc are probing different parts of the same global population, which has metallicity of  $[Fe/H] = -0.9$ .

### 5.10. Scale-length

A further useful constraint on the nature of this disk-like population is its density profile. We proceed by measuring the number  $n_s$  of stars within  $2\sigma$  of the narrow peaks shown in Figure 10 and Figures 16 to 23, and count the number of observed targets  $n_o$  in the CMD selection window, and also the number of available targets  $n_t$  within the selection window that fall into the DEIMOS

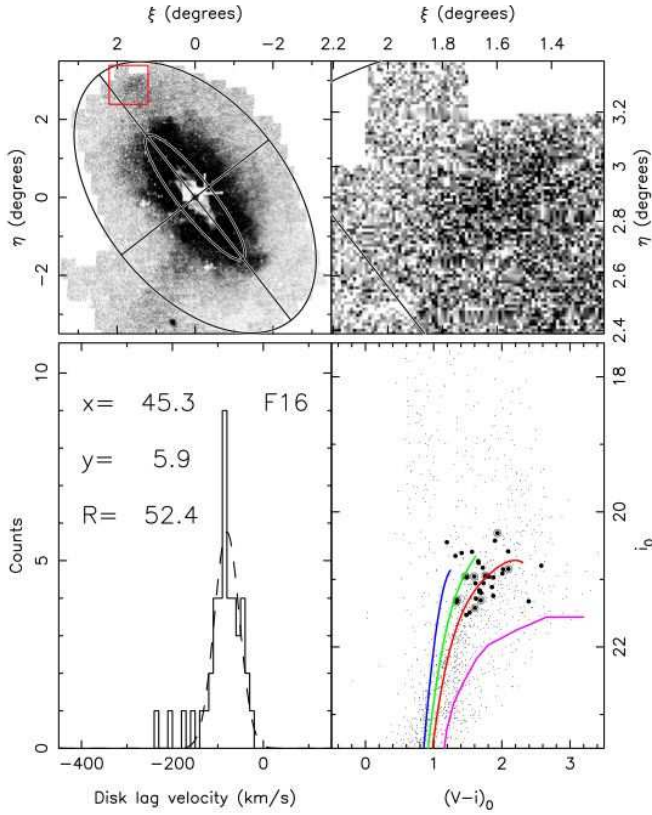


FIG. 23.— As Figure 16, but for field F16. The Gaussian model has  $\bar{v}_{lag} = -80 \text{ km s}^{-1}$  and  $\sigma_v = 27 \text{ km s}^{-1}$  ( $\bar{v}'_{lag} = -65 \text{ km s}^{-1}$ ,  $\sigma_{v'} = 28 \text{ km s}^{-1}$ ).

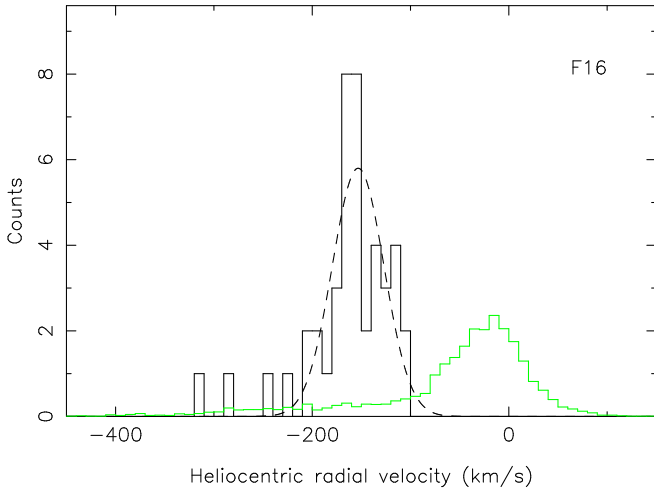


FIG. 24.— The heliocentric velocity distribution of field F16, situated in the low-surface brightness overdensity to the North-east of M31. The green histogram shows the prediction of the Besançon model in an area of the DEIMOS field of view, but corrected for the fact that only 92 stars in the CMD selection window were observed (out of a possible 282). The Besançon model therefore predicts that the Galactic contamination is minimal at heliocentric velocities  $v < -100 \text{ km s}^{-1}$ , which strengthens the results presented in Figure 23.

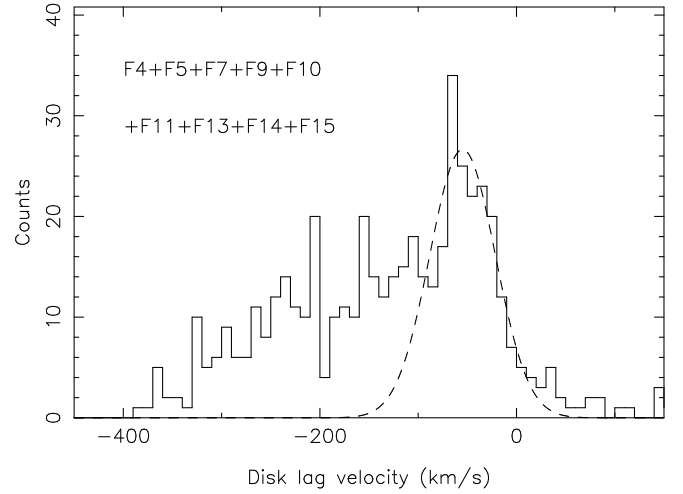


FIG. 25.— The distribution of disk lag velocities for the (non-stream) external fields without a prominent narrow disk-like velocity component; these are: F4, F5, F7, F9, F10, F11, F13, F14 and F15. This combining brings out of the noise, yet again, a narrow velocity peak close to expected velocity of a circularly rotating population. For illustrative purposes only, we have fitted the velocity interval  $-80 \text{ km s}^{-1} < v_{lag} < 50 \text{ km s}^{-1}$  with a Gaussian of mean  $\bar{v} = -55 \text{ km s}^{-1}$  and dispersion  $\sigma_v = 33 \text{ km s}^{-1}$  ( $\bar{v}'_{lag} = -41 \text{ km s}^{-1}$ ,  $\sigma_{v'} = 31 \text{ km s}^{-1}$ ).

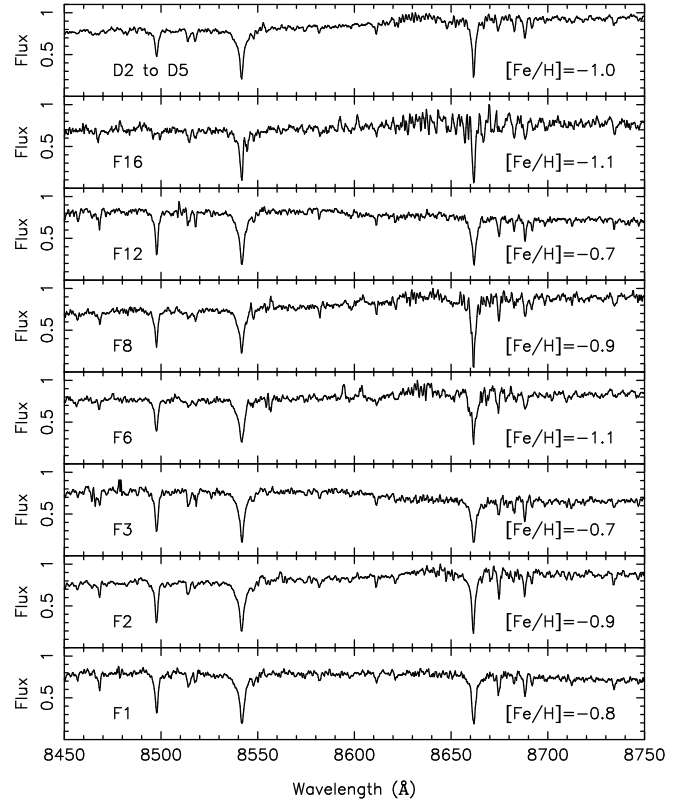


FIG. 26.— Combined spectra for all the stars within  $2\sigma$  of the Gaussian fit. The three Ca II triplet lines at  $8498.02 \text{ \AA}$ ,  $8542.09 \text{ \AA}$ , and  $8662.14 \text{ \AA}$  are the most obvious features of these spectra. The field name is indicated on the left, and derived metallicities on the right of each panel.

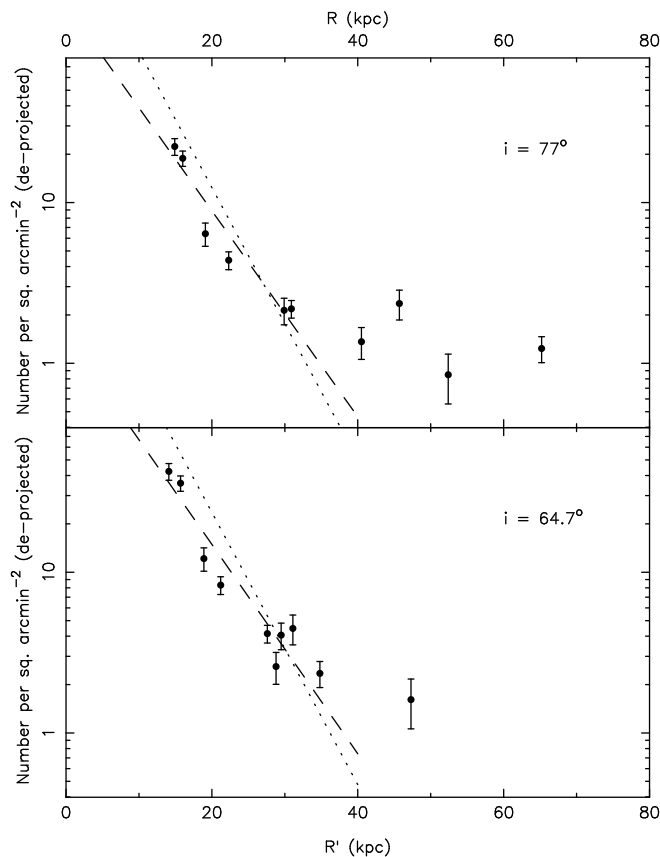


FIG. 27.— The density profile of the extended disk population is displayed in the top panel, isolated by counting kinematically-confirmed stars and scaling by the ratio of possible targets to the total number of stars measured in each field. A disk-plane inclination of  $i = 77^\circ$  is assumed to calculate both the de-projected radius  $R$  and the de-projected surface density. The dashed line shows an exponential fit to the data in the range  $R < 40$  kpc, which implies a scale-length of  $h_R = 6.8 \pm 0.4$  kpc. The dotted line reproduces the fit to the outer major axis profile of Figure 2 ( $h_R = 5.1 \pm 0.1$ ). Field F6 is not included in this plot since it lies on the dwarf galaxy NGC 205, whose stars enhance enormously the number of possible targets in the DEIMOS field. The lower panel shows the same data for  $i = 64.7^\circ$ . The fitted exponential function has scale-length  $h_R = 6.7 \pm 0.3$  kpc. The dotted line again reproduces the fit of Figure 2, corrected for the difference in inclination angle.

field of view. The local density in a field is estimated as  $n_t n_s / n_o - n_b$ , where  $n_b$  is the background density computed from fields at the edge of the survey. The top panel of Figure 27 shows the resulting RGB star density profile, under the assumption of the standard Waltherbos & Kennicutt (1988) inclination angle of  $i = 77^\circ$ . The profile shows an exponential decline to  $R \sim 40$  kpc, at which point there appears to be a break in the relation, with possibly a flat extension from  $\sim 40$  kpc to  $\sim 70$  kpc. Fitting the data at  $R < 40$  kpc, we measure an exponential scale-length of  $h_R = 6.8 \pm 0.4$  kpc. This value is somewhat higher than the  $5.1 \pm 0.1$  kpc scale-length (dotted line) that we fitted earlier to the major axis star-counts. If we instead assume the lower inclination angle calculated in §2 of  $i = 64.7^\circ$  (lower panel), the scale-length drops marginally to  $h_R = 6.7 \pm 0.3$  kpc.

These longer scale-lengths may mean that the population with disk-like kinematics that we have uncovered in

these fields has a slightly different profile to the underlying exponential population revealed in Figure 2, or it may also mean that the inclination of the outer disk is lower than  $i = 64.7^\circ$ . However, it should be recalled that the spectroscopic fields preferentially targeted overdensities detected in the photometric survey, which need not follow closely the medianed major axis profile. Another important property to bear in mind when interpreting Figure 27 is that the velocity distributions in all fields showed narrow peaks at a similar velocity lag. There was no indication of bimodal distributions with a component due to an underlying smooth “normal” disk plus an additional component due to the sub-structure (with the exception of field F2 which we discussed in §5.2). If there were an underlying normal disk population it has identical kinematics to the substructure.

### 5.11. Total luminosity and angular momentum

In terms of its mass fraction, the outer disk is a very significant part of the galaxy. As we have shown in Figure 2, the exponential decline can be followed out to 40 kpc or 7.8 scale-lengths. Approximately 10% of the mass of the M31 disk therefore lies beyond the typical 4 scale-length cutoff (Pohlen, Dettmar & Lütticke 2000). This region contains an even larger fraction of the angular momentum of the disk: assuming a flat rotation curve results in  $\sim 30\%$  of the angular momentum of the disk residing beyond 4 scale-lengths.

### 5.12. H I content

Recently, Thilker et al. (2004a) have presented an analysis of Green Bank Telescope  $\lambda 21$  cm observations of M31 and its environment. Their very high sensitivity of  $2.5 \times 10^{17} \text{ cm}^{-2}$  within a beam-size of 2 kpc allowed them to detect many low-mass H I clouds as well as an extended filamentary component. A careful inspection of their Figure 1, in which the H I data-cube is presented, reveals a spatial overlap between the H I emission and our extended disk fields. Furthermore, the velocities of the H I gas coincide with the peaks of the extended disk velocity distributions found in the present study, though a detailed comparison is not currently possible as the velocity intervals in the map presented by Thilker et al. (2004a) are large ( $34 \text{ km s}^{-1}$ ).

### 5.13. Variations in stellar populations

The color-magnitude diagrams presented in Figures 16–23 show a very similar broad upper RGB, indicating that a similar distribution of stars populates these fields. However, recent work by our group (Ferguson et al. 2005) using very deep photometry from the Advanced Camera for Surveys (ACS) instrument on board the Hubble Space Telescope reveals significant differences in the morphology of the horizontal branch over the inner part of the M31 “halo”. The surveyed fields include small areas of the fields F1, F5, F9, F10, F11 and F12 from the present study. The differences in the horizontal-branch populations testify to the existence of inhomogeneities in the *old* stellar populations in these fields.

## 6. DISCUSSION

Our radial velocity data reveal the presence of an unexpected population, present in almost all the surveyed

fields from  $R = 15$  kpc out to  $\sim 70$  kpc, that lags the H I by at most  $80 \text{ km s}^{-1}$ , and that has a dispersion of  $\sim 20 \text{ km s}^{-1}$  to  $\sim 40 \text{ km s}^{-1}$ . This velocity dispersion is large enough to rule out the possibility that these structures are bound dwarf galaxies. It should be kept in mind that the circularly-rotating disk model that we presented in Figure 7 is very simplistic, and one should expect significant deviations from it, especially on fields at large  $y$  (minor axis distance), where small changes in the inclination of the disk, due for instance to warping, will cause large errors in the disk velocity lag. So the good agreement in the mean velocity of the disk-like peak in each field is all the more surprising. The direction of the effect is such that if the disk is warped so that it is seen less edge-on, the model of Figure 7 will overestimate the rotational velocity, and a population will appear to run ahead of circular motion.

The errors in the model, however, will not affect significantly the fitted  $\sigma_v$  in each field. The variations in  $\sigma_v$  in the outer fields are large, ranging between  $\sigma_v = 15 \text{ km s}^{-1}$  in field F3 and  $\sigma_v = 38 \text{ km s}^{-1}$  in field F8. Field F2 (with  $\sigma_v = 35 \text{ km s}^{-1}$ ) mirrors field F3 about the major axis, so we can see that the differences in velocity dispersion reflect real changes between fields, which are not just due to different projections of the  $R$  and  $\phi$  components of the velocity ellipsoid onto the line of sight.

For the metallicity measurements we are unfortunately forced to co-add the spectra in the velocity peaks to obtain combined spectra of useful signal to noise. This necessarily means that we lose all information on the metallicity dispersion of the populations. Nevertheless, the mean metallicity can be measured reliably, and the derived values in all fields are consistent with the data from each field being drawn from a global population of identical metallicity.

All the DEIMOS fields we present in this paper, except for fields F5 and F7 were positioned on regions of high target density in M31, which is seen as the dark black area in a visual inspection of Figure 1. This corresponds to a surface number density of stars of approximately  $10^4$  degree $^{-2}$  in the RGB selection window defined in §3. The panoramic view of the INT survey provides an invaluable complement to the spectroscopic results. Given the very similar velocity dispersions, disk velocity lags and metallicities of the stars we have identified, it is clear from an inspection of Figure 1 that these populations can be united in a single morphological entity: an extended disk-like structure which has rather remarkable well-defined fragmented sub-structures at its outer edge.

### 6.1. Interpretation of velocity lag

We have found a population that appears to lag the velocity of circular orbits in many fields, but what does this lag represent? A simple answer may be that, in reality, the outer disk is less inclined than we modeled. However, some fraction of the velocity lag must be intrinsic. In an equilibrium disk, a stellar population with non-zero velocity dispersion lags the circular speed; this is known as the asymmetric drift (see, e.g., Binney & Tremaine 1987, their §4.2). We use Eqn. 4-35 of Binney & Tremaine (1987) to estimate the expected asymmetric drift, and adopt their simplifying assumptions taken to calculate the Solar Neighborhood asymmetric drift re-

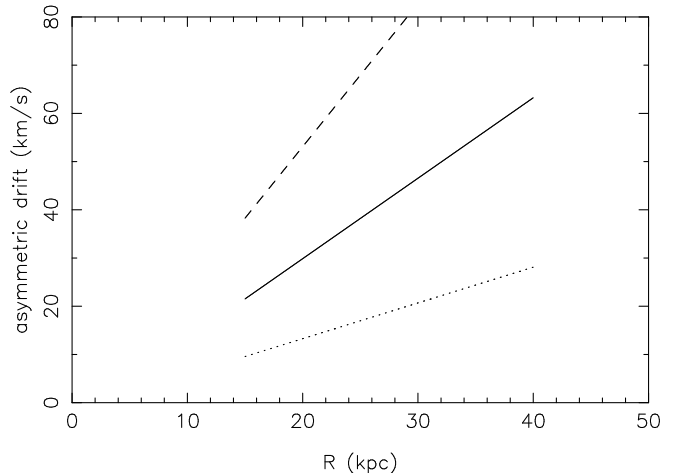


FIG. 28.— The asymmetric drift of a disk population in equilibrium, for three different values of the  $\phi$ -component of velocity dispersion:  $20 \text{ km s}^{-1}$  (dotted line),  $30 \text{ km s}^{-1}$  (continuous line) and  $40 \text{ km s}^{-1}$  (dashed line). A scale-length of  $5.1 \pm 0.1$  kpc, as measured in §2, was adopted.

lation. Figure 28 shows the expected asymmetric drift as a function of radius for disk populations of dispersion  $\sigma_\phi = 20 \text{ km s}^{-1}$  (dotted line),  $\sigma_\phi = 30 \text{ km s}^{-1}$  (continuous line) and  $\sigma_\phi = 40 \text{ km s}^{-1}$  (dashed line). These estimates show that a significant velocity lag should be expected.

However, there are many uncertainties that hinder a direct comparison of these asymmetric drift estimates to the data. First of all, the overdensities targeted in the outer fields are evidently not equilibrium structures, so the asymmetric drift equation need not hold precisely. Apart from the uncertainty in the inclination of the galaxy, there are further uncertainties in the projection of the velocity dispersion ellipsoid, as we discussed in §4.1. A realistic treatment of the asymmetric drift will require data that sample better the extended disk region.

### 6.2. Time-scale for dissolution

With typical sizes of  $\sim 5$  kpc and velocity dispersions of  $\sigma_v \sim 30 \text{ km s}^{-1}$ , the virial mass associated with the sub-structures we discuss in §5 would have to be of the order of  $\sim 10^9 M_\odot$ . However, the total luminosity of these sub-structures is very low, although this is a difficult quantity to measure given the irregular morphology and the difficulty of identifying their spatial limits. For the case of field F16, where the structure is well-separated from M31, the total luminosity is a mere  $3 \times 10^6 L_\odot$ . Thus if these structures are bound, they require a ridiculous mass to light ratio of several hundred in Solar units. They are instead most probably unbound structures dissolving in the global potential of the galaxy.

It is informative to estimate the lifetime of the structures if they are indeed unbound. In this case both the winding due to differential rotation and the velocity dispersion of the structure set a dissolution time-scale. In a potential with a flat rotation curve of velocity  $v_c$ , an unbound structure at galactocentric radius  $R$  becomes smeared out by an extent equal to its initial size in a time  $R/v_c$ , i.e. in 170 Myr at  $R = 40$  kpc for the case of M31 (taking  $v_c = 240 \text{ km s}^{-1}$ ). Alternatively, if we

consider just the effect of the expansion of the stellar population due to its velocity dispersion unconstrained by self-gravity, with a velocity dispersion of  $\sim 30 \text{ km s}^{-1}$ , a structure of size 5 kpc will double in size in 170 Myr, fortuitously the same time estimated before. These simple arguments give an order-of-magnitude estimate of the the survival time of the structures, and strongly suggest that they cannot be long-lived.

### 6.3. Age of population

Brown et al. (2003) present extremely deep photometry with the ACS camera for a field on the minor axis of M31. The location of this field, indicated in Figure 4 with a small square, lies at a projected radius of only  $y = -11.4 \text{ kpc}$ . The corresponding de-projected radius is  $R = 53 \text{ kpc}$ , beyond the break in the surface density profile of Figure 27. However, a tiny  $5^\circ$  warp in the extended disk would bring the field into the  $R < 40 \text{ kpc}$  region. In their data, Brown et al. find evidence for a 30% component of intermediate age stars (6–8 Gyr) with metallicity  $[\text{Fe}/\text{H}] > -0.5$ , though they claim a similar-quality fit for a population of metallicity  $[\text{Fe}/\text{H}] > -1.0$ . Given that this is the youngest component in that field, and has comparable metallicity, it is possible that the intermediate-age population whose age they constrain is the extended disk. However, a definitive measure of the age of the population will require resolving the main-sequence turnoff in fields where we are sure the the extended disk population is present.

### 6.4. Formation scenarios

How did the extended disk form? Several possibilities present themselves.

- **Formation by the accretion of many small sub-galactic structures.** This scenario would explain naturally the lumpy sub-structure seen at the edge of the extended disk, as well as the differences in the velocity dispersion and the variations in the old stellar populations between fields. However, the chemical homogeneity of the material argues against this possibility, since the different accreted galaxies would likely have a range of different metallicities, depending on their mass and star-formation history. Admittedly, the metallicity measurements we present above give only the mean of the population, and in the central regions of M31, considerable mixing must have taken place. Nevertheless, it is surprising to find the same mean abundance even in the outermost sub-structures. A further problem with this scenario is the disk-like kinematics. A substantial mass is required for dynamical friction to affect the orbit of a galaxy satellite ( $> 10^8 M_\odot$ , Binney & Tremaine 1987) which has to become circularized *before* being disrupted in order to give rise to a final structure with disk-like kinematics. Another problem is the disk-like distribution of debris. Though accretion in the disk plane does appear to be favored (Peñarrubia, Kroupa & Boily 2002), the accretion of a large number of halo objects is expected to give rise to a distribution closer to that of a spheroidal stellar halo than a disk. Even the thick disk component in the Abadi et al. (2003) simulation, in which  $\sim 50\%$

is formed by accretion, is a very thick component of axis ratios  $\sim 1 : 3$  and scale-length of 4.5 kpc (our measurements from their Figures 1 and 3). Forming the extended disk observed in M31 in this way will certainly be a challenge for modelers.

- **Formation from stars accreted in a single large merger.** Here we envisage the assimilation of a whole M33-sized galaxy in a single merging event. Accreting 10% of the total mass of a galaxy counts as a significant merger, affecting the morphology of the larger galaxy. However, given that the bulk of the interaction took place long ago, possibly 6–8 Gyr in the past (corresponding to  $z \sim 1$ ), the progenitor of M31 would have been considerably less massive at that time (Hammer et al. 2005), and the resulting interaction would likely be termed a “major merger” after which Andromeda would have been globally reshaped. Thin disks are easily heated up by mergers (Tóth & Ostriker 1992; Velazquez & White 1999), so this scenario makes a testable prediction that stars in the inner disk of M31 that formed before the merger should have a much larger scale-height than the younger thin disk. The advantage of this proposition is that it accounts naturally for the uniform mean abundances measured in the different fields. It is questionable that such a merger could have given rise to a population with disk-like morphology and kinematics, since typical disk galaxy collisions result in elliptical end-products (e.g., Hernquist 1992). However, new simulations by Springel & Hernquist (2005) cast doubt on the inevitability of forming elliptical galaxies from such collisions, showing that disk galaxies may form even in equal mass mergers if the progenitors are gas dominated. Further numerical experiments are required to establish whether a disk as extended as the one seen around M31 can be formed in this way.
- **Formation induced by a single large merger.** This scenario would be similar to the previous one, but the stellar population of the accreted galaxy would end up populating the bulge or other spheroidal component of M31. This is perhaps consistent with the presence of a double nucleus in that galaxy (Lauer et al. 1993). However the interaction itself could have triggered star-formation on a massive scale in the pre-existing gaseous disk of M31, with gas accreted from the satellite contributing to the enrichment. This possibility could explain the disk-like structure and kinematics, and has the testable prediction that its constituent stars should be no older than the interaction itself. The homogeneity in mean abundance over the structure could be explained by star-formation being limited very rapidly before chemical enrichment could take place. Such a rapid formation of the disk in this way is similar to what is deduced for  $\sim 1 \text{ mJy}$  sub-mm sources at  $z \sim 2$  with star-formation rates of  $\sim 100 M_\odot/\text{yr}$  (Chapman et al. 2003; Greve et al. 2005). Nevertheless, this scenario is also problematic, as it is hard to reconcile with the variations in the velocity dispersion between fields.

A concern with the last two scenarios is that the substructures that we see on the outskirts of the extended disk now are short-lived features that will soon disappear ( $\ll 1$  Gyr). This means that we would be observing the system at a special time at the very tail-end of the merging process. A further problem is the constraint on the size of a past major merger set by the existence of a population of thin disk globular clusters that has recently been discovered in M31 by Morrison et al. (2004). Those authors infer that no more than 10% of the mass of the disk could have been accreted in a single merger since the formation of the clusters. The time of formation of the clusters is currently poorly constrained, though they find no reason why the clusters should be significantly younger than those of the Milky Way. Measuring the ages of these objects will help greatly in distinguishing between the above scenarios.

### 6.5. Possible connection to NGC 205?

As we noted in §5.4, if stars become unbound from NGC 205, we would observe them in field F6 with kinematic properties very close to that of disk material. Likewise, if McConnachie et al. (2004b) were correct in identifying the arc-like structure to the North of M31 as a tidal stream from NGC 205, this tidal debris, which is located in fields F8 and F9, would also have disk-like kinematics.

This raises the possibility that NGC 205 is connected to the extended disk structure, either as the direct supplier of stars, or as the remnant of the ancient structure which created the extended disk. It is interesting to note in this context that the mean metallicity of NGC 205 has been measured to be  $[\text{Fe}/\text{H}] \sim -0.9$  (Mould, Kristian & Da Costa 1984), identical to the mean spectroscopic measurements from the fields presented in this survey.

A counter-argument however, is that recent estimates for the distance to NGC 205 indicate that it is behind M31, being at a distance of  $824 \pm 27$  kpc (McConnachie et al. 2005), compared to  $785 \pm 25 - 40.6 \sin(i)$  kpc for the M31 disk at the location of NGC 205. The difference in distance is therefore  $79 \pm 37$  kpc, little over  $2\sigma$ , although we are probably grossly overestimating the uncertainties, since a differential distance measurement is expected to be much more accurate.

However, this need not rule out the connection with NGC 205. If the dwarf galaxy were indeed  $\sim 80$  kpc beyond the foreground disk on the near side of M31, it would be  $\sim 40$  kpc behind M31, at a location  $\sim 17$  kpc above the plane of the disk on the far side of that galaxy.

### 6.6. Comparison to Hurley-Keller et al. (2004)

Hurley-Keller et al. (2004) have presented an analysis of the kinematics of 135 planetary nebulae in the disk and inner halo of M31. They find the surprising result that a standard model for the thin disk, thick disk and bulge cannot reproduce the observed PNe kinematics at major axis distances of 15 kpc to 25 kpc. In order not to introduce the presence of an additional component, they invoke Occam's razor to alter the parameters of the bulge, deducing that the bulge must rotate rapidly at large distances. We re-assess their data in the light of the discovery of the additional extended disk population. Figure 29 shows the positions of the 135 PNe in their survey. Stars

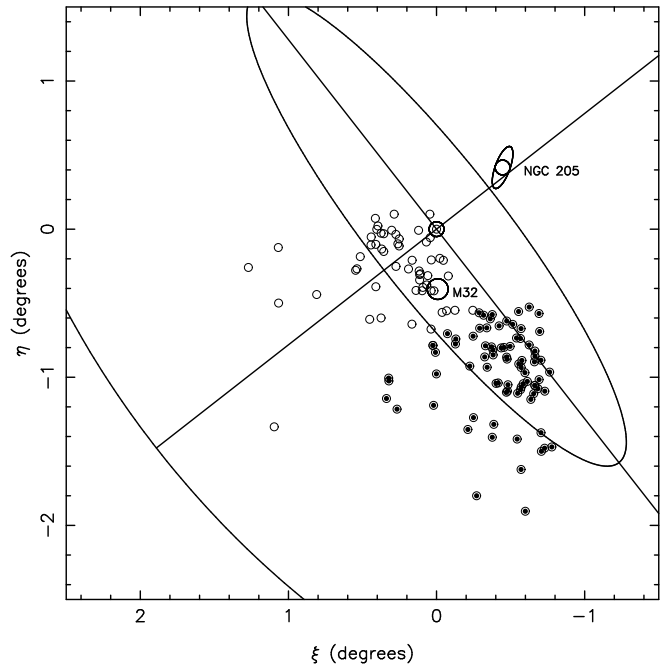


FIG. 29.— The location of the PNe from Hurley-Keller et al. (2004) with respect to M31; the lines and ellipses from Figures 1 and 4 are reproduced to show the scale. The small open circles show the full sample of 135 PNe, while our chosen sub-sample of 77 objects with  $|x| > 8$  kpc are indicated with filled circles.

close to the centre of M31 are a complex mix of populations, so we investigate the sub-sample with  $|x| > 8$  kpc, which are displayed as filled circles. The distribution of velocity lags is shown in Figure 30. We fit this distribution for  $v_{lag} > -150 \text{ km s}^{-1}$  using a maximum-likelihood algorithm, to account for the velocity measurement uncertainties quoted by Hurley-Keller et al. (2004) as well as the disk model uncertainties (from Figure 8). The resulting Gaussian model has  $\bar{v}_{lag} = -52 \text{ km s}^{-1}$  and  $\sigma_v = 44 \text{ km s}^{-1}$ , very similar to the fit in Figure 10. Further analysis is necessary to establish conclusively whether the existence of the extended disk alleviates the need for a rapidly rotating outer bulge as suggested by Hurley-Keller et al. (2004).

### 6.7. Globular clusters

A population of massive globular clusters has recently been found in the disk of M31 (Fusi Pecci et al. 2005). These objects are scattered around the outskirts of the inner disk at distances of  $\sim 20$  kpc, and have very blue colors, with color indices indicating a young age of  $\sim 2$  Gyr. The population is also very significant, accounting for  $\gtrsim 15\%$  of the globular cluster system of that galaxy. This population of young clusters rotates rapidly, possessing kinematics similar to that of the disk. A further piece of relevant information is provided by the recent discovery of the globular cluster Bologna 514 (Huxor et al. 2003; Galleti et al. 2005), which is situated close to the South-western major axis of M31 at a projected distance of 55 kpc, almost exactly on the outer ellipse marked in Figures 1 and 4. The rotation model of Figure 7 gives a disk-lag velocity of this globular cluster

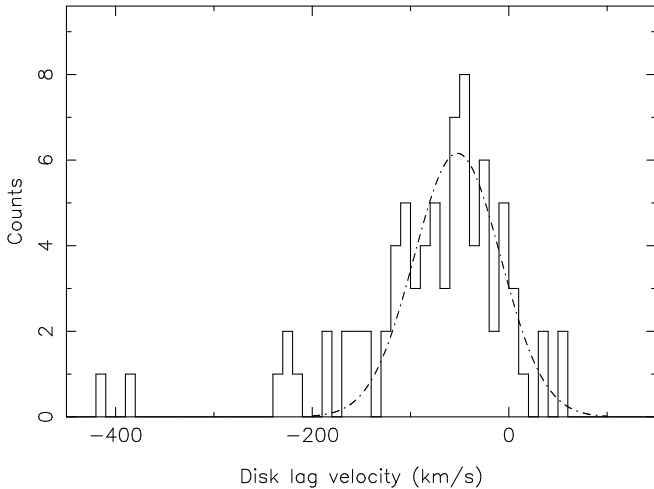


FIG. 30.— The distribution of disk lag velocities of the Hurley-Keller et al. (2004) PNe with  $|x| > 8$  kpc. A maximum-likelihood Gaussian fit to the data in the interval  $-150 \text{ km s}^{-1} < v_{lag} < 100 \text{ km s}^{-1}$  is also shown, for which both the estimated velocity uncertainties from Hurley-Keller et al. (2004) as well as the uncertainties in the disk rotation model (from Figure 8) have been taken into account. We fit a Gaussian mean velocity lag of  $\bar{v}_{lag} = -52 \text{ km s}^{-1}$  and dispersion  $\sigma_v = 44 \text{ km s}^{-1}$  ( $\bar{v}'_{lag} = -44 \text{ km s}^{-1}$ ,  $\sigma_{v'} = 46 \text{ km s}^{-1}$ ). The same low dispersion disk-like population as discovered in our DEIMOS fields is also present here.

of  $v_{lag} = -70 \text{ km s}^{-1}$  ( $v'_{lag} = -53 \text{ km s}^{-1}$ ).

Though it is tempting to speculate on a possible connection between these globular clusters and the extended disk, the metallicities of the clusters appear to be much lower than the  $[\text{Fe}/\text{H}] = -0.9$  we measure for the structures in this study. However, as pointed out by Fusi Pecci et al. (2005), the metallicities of these globular clusters could be higher if they are of younger age than the typical halo cluster. Further observations are needed to establish the age of these M31 disk clusters, and their relation to the extended disk.

#### 6.8. A connection with the thick disk?

Several edge-on galaxies have been found to possess a flattened component with a much larger scale-height than the thin disk (Dalcanton & Bernstein 2002) probably indicating the presence of a thick disk. Recently, two of the sample of Dalcanton & Bernstein (2002) were observed spectroscopically by Yoachim & Dalcanton (2005), who found the thick disk to be rotating very slowly in one case and counter-rotating in the other. This result shows that thick disks can have completely different kinematics from the thin disk, although this is not the case for the Milky Way. The fact that the extended disk we find around M31 has a low velocity dispersion, and follows circular orbits closely thus behaving kinematically like a thin disk, as well as having a very similar scale-length to the thin disk, suggests a close link with that component, and argues against association with the thick disk of Andromeda. It should be noted, however, that it has not yet been shown that Andromeda does indeed possess a thick disk. The present dataset may allow us to detect the thick disk, but we will return to this issue in a future contribution.

#### 6.9. Extended disks in other galaxies?

Our group has also been attempting to unravel the formation history of the Milky Way (Ibata et al. 2001a, 2002), with similar goals to our study of M31. Following up on the discovery of a peculiar halo structure in the SDSS (Newberg et al. 2002), we showed that the Milky Way is enveloped in a Ring-like distribution of old stars that lie at Galactocentric distances of  $\sim 20$  kpc, well beyond the edge of the Galactic disk (Ibata et al. 2003). A subsequent analysis of asymmetries in the 2MASS survey revealed a strong enhancement of stars at the edge of the Galactic disk, which we interpreted as an accreted dwarf galaxy fragment (Martin et al. 2004a,b; Bellazzini et al. 2004, see also Rocha-Pinto et al. 2005); a connection with the ring-like structure is possible, though not proven. However, this “Galactic Ring” or “Galactic Anticenter Stellar Structure” (Crane et al. 2003) is not the only stellar population with disk-like kinematics that lies beyond the rim of the Milky Way thin-disk: recently Majewski et al. (2004) and Rocha-Pinto et al. (2004) have uncovered a further stellar structure located at a distance of  $\sim 40$  kpc and which spans a huge angle on the sky. These findings indicate that the outer regions of the Galactic plane have a similar messy flattened structure to what is observed in M31 (Figure 1).

A possible young counterpart to the “extended disks” in the Milky Way and M31 has been seen in some more distant galaxies. GALEX observations of M83 (Thilker et al. 2004b) have revealed an extended population of UV sources (OB stars) beyond the inner disk (though at much smaller radius than the structure we detect in M31), while several galaxies are known to exhibit H II regions to extremely large radii (Ferguson et al. 1998). Thus it appears that there may exist an additional component to spiral galaxies, a putative “extended-disk”. The implications for galaxy formation are profound: the inhomogeneous spatial distribution and moderately high metallicity suggests an origin in multiple accretions, yet accreted fragments, which are the building blocks of galaxies, do not give rise to these huge extended disks in current simulations.

#### 7. CONCLUSIONS

We have presented an analysis of a large survey of the Andromeda galaxy with the Keck/DEIMOS spectrograph based on targets selected from a panoramic survey with the INT Wide Field Camera. A huge rotating structure that follows an exponential density law with scale-length  $5.1 \pm 0.1$  kpc is detected out to a de-projected distance of  $\sim 40$  kpc, with sub-structures continuing out even further in radius. All of the photometric sub-structures that were targeted for spectroscopic follow-up participate in the same disk-like movement. The velocity dispersion is low, typically  $30 \text{ km s}^{-1}$ . These properties indicate that the population is a huge extended stellar disk. The color dispersion on the RGB of stars that belong to this structure is broad, implying that a wide metallicity range is present. Spectroscopic measurements of the mean metallicity give  $[\text{Fe}/\text{H}] = -0.9 \pm 0.2$ . No significant radial trend in either kinematics or metallicity is found, although deep ACS photometry in several of the DEIMOS fields reveals variations in the horizontal branch morphology over the galaxy, indicating that the stellar population of the most ancient stars differ between

fields. We estimate that  $\sim 10\%$  of the luminous mass of the Andromeda disk resides in this extended disk component, beyond the 4 scale-length cutoff observed in most galaxies. However, this region may account for  $\sim 30\%$  of the total angular momentum of the galaxy.

The spatial sub-structures that form the outer edge of this system are almost certainly no longer gravitationally bound and will disappear as spatially coherent entities within  $\sim 200$  Myr. However, the existence of these sub-structures indicates a formation mechanism by mergers, and implies that the extended disk is still forming, although we seem to be observing it at the very tail end of its formation period. It is unclear at this point whether the extended disk was formed by multiple accretion events or by a single large event, though the latter possibility appears more plausible given the present data.

Many questions remain to be answered. Is the extended disk a continuation of the thin disk, or is it a separate component? Was the merger, or were the mergers, that formed the extended disk responsible for the formation of the  $R^{1/4}$ -law halo of Andromeda? Why is the extended disk closely aligned with the thin disk? Why is it not extremely warped?

The surface brightness of this structure, 27–31 mag/arcsec<sup>2</sup> in its outer regions, places it beyond what would be classified as “disk” in more distant systems. Though such faint surface brightness levels are extremely challenging to observe, by resolving individual stars it will be possible to ascertain whether the extended disk is a particularity of M31 or whether similar components are present in other galaxies. Further work is also needed in the Milky Way to study the distant stellar populations hidden by foreground populations in the Galactic plane, and to understand the nature of the structures recently unveiled at the edge of the Galactic disk and beyond (Newberg et al. 2002; Ibata et al. 2003; Martin et al. 2004a,b; Majewski et al. 2004; Rocha-Pinto et al. 2004, 2005), and their relation to the vast extended disk in the Andromeda galaxy.

#### ACKNOWLEDGEMENTS

RI would like to thank Françoise Combes, and Bernd Vollmer for very helpful comments and suggestions. SCC acknowledges support from a NASA. GFL acknowledges support through the ARC DP0343508.

#### REFERENCES

- Abadi M., Navarro J., Steinmetz M. & Eke V. 2003, ApJ 597, 21  
 Avila-Reese, V., Firmani, C., Hernández, X. 2001, in *New Questions in Stellar Astrophysics: The Link between Stars and Cosmology*, eds. M. Chavez, A. Bressan, A. Buzzoni, & D. Mayya (Dordrecht: Kluwer)  
 Bellazzini, M., Ibata, R., Monaco, L., Martin, N., Irwin, M., Lewis, G. 2004, MNRAS 354, 1263  
 Binney, J. & Tremaine, S. 1987, *Galactic Dynamics*, Princeton University Press, Princeton  
 Bland-Hawthorn, J., Vlajić, M., Freeman, K., Draine, B. 2005, ApJ in press, astro-ph/0503488  
 Brinks, E., Burton, W. 1984, A&A 141, 195  
 Brown, T., Ferguson, H., Smith, E., Kimble, R., Sweigart, A., Renzini, A., Rich, M., VandenBerg, Don A., 2003, ApJ 592, 17L  
 Carretta, E., Gratton, R. 1997, A&AS 121, 95  
 Chapman, S., Blain, A., Ivison, R., Smail, I. 2003, Nature 422, 695  
 Chiba, M., Beers, T. 2000, AJ 119, 2843  
 Crane, J., Majewski, S., Rocha-Pinto, H., Frinchaboy, P., et al. 2003, ApJ 594, 119  
 Dalcanton J., Bernstein R., 2002, AJ 124, 1328  
 Davis, M., et al. 2003, Proc. SPIE, 4834, 161  
 Dehnen, W. & Binney, J., 1998, MNRAS 298, 387  
 Durrell, P., Harris, W., Pritchett, C. 2001, AJ 121, 2557  
 Durrell, P., Harris, W., Pritchett, C. 2004, AJ 128, 260  
 Evans, N., Wilkinson, M., Guhathakurta, P., Grebel, E., Vogt, S., 2000, ApJ 540, 9L  
 Ferguson, A., Wyse, R., Gallagher, J., Hunter, D. 1998, ApJ 506, 19  
 Ferguson, A., Irwin, M., Ibata, R., Lewis, G., Tanvir, N., 2002, AJ 124, 1452  
 Ferguson, A., Johnson, R., Faria, D., Irwin, M., Ibata, R., Johnston, K., Lewis, G., Tanvir, N. 2005, ApJ 622, 109L  
 Fusi Pecci, F., Bellazzini, M., Buzzoni, A., De Simone, E., Federici, L., Galletti, S. 2005, astro-ph/0503188  
 Galletti, S., Bellazzini, M., Federici, L., Fusi Pecci, F. 2005, astro-ph/0503206  
 Gilmore, G., Reid, N. 1983, MNRAS 202, 1025  
 Greve, T., Bertoldi, F., Smail, I., Neri, R., Chapman, S., Blain, A., Ivison, R., Genzel, R., Omont, A., Cox, P., Tacconi, L., Kneib, J.-P. 2005, MNRAS in press, astro-ph/0503055  
 Hammer, F., Flores, H., Elbaz, D., Zheng, X., Liang, Y., Cesarsky, C. 2005, A&A 430, 115  
 Hernquist, L. 1992, ApJ 400, 460  
 Holland, S., Fahlman, G. G., Richer, H. B., 1996, AJ, 112, 1035  
 Hurley-Keller, D., Morrison, H., Harding, P., Jacoby, G. 2004, ApJ 616, 804  
 Huxor, A. Tanvir, N., Irwin, M., Ferguson, A., Ibata, R., Lewis, G., Bridges, T. 2003, in *Satellites and Tidal Tails*, eds. F. Prada, D. Martinez-Delgado, T. Mahoney, ASP vol. 327  
 Huxor, A. Tanvir, N., Irwin, M., Ibata, R., Collett, J., Ferguson, A., Bridges, T., Lewis, G. 2005, astro-ph/0412223  
 Ibata R., Lewis G., Irwin M., Totten E. & Quinn T., 2001a, ApJ 551, 294  
 Ibata, R., Irwin, M., Lewis, G., Ferguson, A., Tanvir, N., 2001b, Nature 412, 49  
 Ibata R., Lewis G., Irwin M. & Cambrésy L., 2002, MNRAS 332, 921  
 Ibata, R., Irwin, M., Lewis, G., Ferguson, A., Tanvir, N. 2003, MNRAS 340, 21  
 Ibata, R., Chapman, S., Ferguson, A., Irwin, M., Lewis, G. 2004, MNRAS 351, 117  
 Irwin, M., Trimble, V. 1984, AJ 89, 83  
 Katz, N. & Gunn, J. 1991, ApJ 377, 365  
 Kennicutt, R. 1989, ApJ 344, 685  
 Klypin, A., Kravtsov, A., Valenzuela, O., Prada, F. 1999, ApJ 522, 82  
 Klypin, A., Zhao, H.-S., Somerville, R., 2002, ApJ 573, 597  
 van der Kruit, P., Searle, L. 1981, A&A 95, 105  
 Lauer, T., Faber, S., Groth, E., Shaya, E., Campbell, B., Code, A., Currie, D., Baum, W., Ewald, S., Hester, J., Holtzman, J., Kristian, J., Light, R., Ligynds, C., O’Neil, E., Westphal, J. 1993, AJ 106, 1436  
 Loinard, L., Allen, R., Lequeux, J. 1995, A&A 301, 68  
 Martin, N. F., Ibata, R., Bellazzini, M., Irwin, M., Lewis, G., Dehnen, W. 2004a, MNRAS 348, 12  
 Martin, N., Ibata, R., Conn, B., Lewis, G., Bellazzini, M., Irwin, M. 2004b, MNRAS 355, 33  
 Majewski S., et al. 2004, ApJ 615, 738  
 McConnachie, A., Irwin, M., Ferguson, A., Ibata, R., Lewis, G., Tanvir, N., 2004a, MNRAS 350, 243  
 McConnachie, A., Irwin, M., Lewis, G., Ibata, R., Chapman, S., Ferguson, A., Tanvir, N. 2004b, MNRAS 351, 94  
 McConnachie, A., Irwin, M., Ibata, R., Lewis, G., Ferguson, A., Tanvir, N. 2005, MNRAS, astro-ph/0410489  
 Moore, B., Ghigna, S., Governato, F., Lake, G., Quinn, T., Stadel, J., Tozzi, P. 1999, ApJ 524, L19  
 Morrison, H., Harding, P., Perrett, K., Hurley-Keller, D. 2004, ApJ 603, 87  
 Mould, J., Kristian, J., Da Costa, G. 1984, ApJ 278, 575  
 Newberg, H., et al. 2002, ApJ 569, 245  
 Peñarrubia, J., Kroupa, P., Boily, C. 2002, MNRAS 333, 779  
 Pohlen, M., Dettmar, R., Lütticke, R. 2000, A&A 357, 1  
 Reitzel, D., Guhathakurta, P. 2002, AJ 124, 234

- Reitzel, D., Guhathakurta, P., Rich, M. 2004, AJ 127, 2133
- Robin, A., Reylé, C., Derrière, S., Picaud, S. 2004, A&A 416, 157
- Rocha-Pinto, H., Majewski, S., Skrutskie, M., Crane, J., Patterson, R. 2004, ApJ 615, 732
- Rocha-Pinto, H., Majewski, S., Skrutskie, M., Patterson, R. 2005, astro-ph/0504122
- Ruphy, S., Robin, A., Epchtein, N., Copet, E., Bertin, E., Fouque, P., Guglielmo, F. 1996, A&A .313L..21R
- Rutledge, G., Hesser, J., Stetson, P. 1997, PASP 109, 883
- Schaye, J. 2004, ApJ 609, 667
- Schlegel, D., Finkbeiner, D., Davis, M. 1998, ApJ 500, 525
- Springel, V., Hernquist, L. 2005, ApJ 622, L9
- Steinmetz, M. & Müller, E. 1995, MNRAS 276, 549
- Summers, F. 1993, Ph.D. Thesis, University of California, Berkeley
- Thilker, D., Braun, R., Walterbos, R., Corbelli, E. Lockman, F., Murphy, E., Maddalena, R. 2004a, ApJ 601, 39L
- Thilker, D., et al. 2004b, astro-ph/0411306
- Tóth, G., Ostriker, J. 1992, ApJ 389, 5
- Velazquez, H., White, S. 1999, MNRAS 304, 254
- Walterbos, R., Kennicutt, R. 1987, A&AS 69, 311
- Walterbos, R., Kennicutt, R. 1988, A&A 198, 61
- Walterbos, R., Braun, R. 1994, ApJ 431, 156
- Wilkinson, M., Kleyna, J., Evans, N., Gilmore, G., Irwin, M., Grebel, E. 2004, ApJ 611, 21
- Yoachim, P., Dalcanton, J. 2005, astro-ph/0501394
- Zucker, D. et al. 2004, ApJ 612, 117L